

Modulation enhanced localization microscopy improves precision with factor five

P.J. Sterrenburg

Master of Science Thesis

Modulation enhanced localization microscopy improves precision with factor five

MASTER OF SCIENCE THESIS

For the degree of Master of Science in Systems and Control at Delft
University of Technology

P.J. Sterrenburg

August 20, 2020

Faculty of Mechanical, Maritime and Materials Engineering (3mE) · Delft University of
Technology



Copyright © Delft Center for Systems and Control (DCSC)
All rights reserved.



Abstract

Recently, several methods were introduced that combine the powers of Structured Illumination Microscopy (SIM) and Single Molecule Localization Microscopy (SMLM). This results in a powerful instrument that enables researchers to reconstruct images with a resolution improvement of a factor two compared to SMLM. In this thesis I show that increasing the number of phase steps in structured illumination improves the precision improvement. Furthermore, I show that for photo-activated fluorescent labels, we can amplify and exploit the non-homogeneous resolution of patterned illumination by additionally making use of patterned activation (PA-SIMFLUX). Simulations show an improvement of 4.78 compared to SMLM in the case of uniform illumination.

I have designed a microscope setup using two Digital Micromirror Devices (DMDs). This optical setup enables DMD-SIMFLUX with nine phase steps per direction and perform with a frame rate of 440fps, currently limited by the frame rate of the camera. The pattern pitch of the excitation light is 231nm, whereas the pitch of the activation light is 233nm. To finish the assembly of this microscope, I present a plan to finalize the alignment of the illumination path, as well as controlling the polarization for the desired interference patterns.

To assess the timing feasibility of the experiments and create a benchmark for the precision, a PALM-TIRF setup with uniform illumination was used based on the work of Kwakwa et al. in [1]. A benchmark was set for 10nm in uniform illumination. The on-time of the photo-activatable dye PA-JF646 enables PA-SIMFLUX experiments with three non-equidistant phase steps. The on-time of the STORM dye Alexa-647 limits the amount of phase steps we can use for DMD-SIMFLUX or lead to discarding a large portion of the blinking data.

Table of Contents

Preface	xi
1 Introduction	1
1-1 Fluorescence microscopy	1
1-1-1 Fluorescence	1
1-1-2 Fluorescence in microscopy	2
1-2 Point spread function and resolution	3
1-3 Super-resolution microscopy	4
1-4 Total Internal Reflection Fluorescence Microscopy	5
1-5 Precision improvement using structured illumination light	8
1-6 Thesis topic	8
2 Theoretical background	11
2-1 Maximum likelihood estimation	11
2-1-1 PSF model	11
2-2 Fisher information and Cramer Rao Lower Bound	12
2-3 CRLB and patterned illumination	12
2-4 Fourier optics	13
2-4-1 Propagation and diffraction	14
2-4-2 Lens as a Fourier Transformer	15
2-4-3 Telescope system	15
2-4-4 High NA focusing	15
2-5 Polarization of light	17
2-5-1 Measuring the polarization state	17
2-6 Digital Micromirror Devices	18

3	Simulations and optical design	21
3-1	Precision improvement with structured illumination	21
3-2	Increased precision improvement with patterned activation	23
3-3	Design of the optical setup	25
3-3-1	Illumination light path	26
3-3-2	Photo-activation light path	28
3-4	Alignment of the system	29
3-5	Polarization control	29
3-5-1	Aligning the polarization	30
3-6	Timing of the imaging experiment	31
4	Experimental methods	33
4-1	Benchmarking SMLM	33
4-1-1	Comparison of TIRF setups	33
4-1-2	Analysis of precision	35
4-2	Calibration of the DMD-SIM setup	37
4-2-1	Aligning the excitation focus	37
4-2-2	Distribution of illumination energy in back focal plane	38
4-2-3	Calibration of the pitch and phase of the illumination pattern	39
4-2-4	Calibration of the activation pattern	40
4-3	On-time analysis of fluorophores	40
4-3-1	Sample preparation	41
5	Results	43
5-1	Comparison of TIRF setups	43
5-2	On-time analysis	44
5-2-1	On-time of Alexa-647	44
5-2-2	On-time of PhotoActivatable JF-646	46
5-2-3	Feasibility for use in modulation enhanced localization microscopy	47
5-3	Simulations of precision improvement with DMD setup	48
6	Roadmap to alignment	51
6-1	Laser coupling alignment	51
6-2	Ensure linear polarization and controlling the polarization state	52
6-3	Aligning the optical path	53
6-4	Positioning the lenses	53
6-5	Ensuring equal intensity distribution	53
6-6	Assessment of polarization at sample plane	54

7	Conclusions and outlook	55
7-1	Conclusions and outlook	55
7-1-1	Conclusion	55
7-1-2	Outlook	55
A	Protocol for Glucose Oxidase buffer	57
B	Sample preparation	59
B-1	Aliquotting dry photo-activatable fluorophores	59
B-2	Sample preparation	59
	Bibliography	61

List of Figures

1-1	Jablonski diagram and Stokes-shift of a fluorophore	2
1-2	Optical setup for fluorescence microscopy	2
1-3	Diffraction pattern of a circular aperture	3
1-4	Rayleigh's resolution criterion	4
1-5	The imaging pipeline to reconstruct a super-resolution image from the raw data .	5
1-6	Difference between epifluorescence imaging and TIRF imaging	6
1-7	Annular pupil for TIRF imaging	7
1-8	Optical setup and working principle of SIMFLUX	8
1-9	DMD-SIM setup	9
2-1	Transformation of spatial frequencies to spatial coordinates	14
2-2	Coordinate transformation for high NA focusing	16
2-3	Individual pixels of a DMD	18
2-4	DMD as a blazed grating	19
3-1	Precision improvement in SIMFLUX with two phase steps	22
3-2	Precision improvement in SIMFLUX with three phase steps	23
3-3	Precision improvement with three non-equal phase steps in patterned illumination	24
3-4	Overview of selective activation	25
3-5	Optical design of the DMD setup	26
3-6	Different planes of the excitation path of the DMD setup	26
3-7	Diffraction from the projected square wave on the DMD to the intermediate plane	27
3-8	Diffraction pattern in the Fourier plane of lens 1	27
3-9	Intensity profile of the back focal plane	28
3-10	The sinusoidal signal on the sample plane of the objective	28

3-11	The relation between the orientation of linearly polarized light and the modulation contrast	30
3-12	Schematic overview of the integration of the LCVR	31
4-1	Figure of the custom PALM-TIRF setup that we built	34
4-2	Comparison of two microscope towers	35
4-3	Camera calibration of the DMD setup	36
4-4	The alignment of the excitation path	37
4-5	Finding the right axial position of the SIM pattern.	38
4-6	Laser energy distribution between the two diffraction peaks	38
4-7	Estimation of the pattern pitch	39
4-8	Spectra of fluorescent dyes and dichroic mirror	40
4-9	Single frame of the blinking data from a 350x350 pixel field of view	41
5-1	Manually counted on-times of STORM dye Alexa-647	45
5-2	processed on-time of STORM dye Alexa-647	45
5-3	Manually counted on-times of PALM dye PA-JF646	46
5-4	Processed on-times of PALM dye PA-JF646	47
5-5	Simulated improvement with perfect modulation contrast	48
5-6	Simulated improvement with a modulation contrast of 0,95	49
5-7	Simulated improvement with a modulation contrast of 0,90	50
6-1	Fiber coupling of the illumination laser	52
B-1	Filling the volume with buffer solution	60
B-2	Sealing off the sample with Picodent Twinsil	60

List of Tables

5-1	Comparison of localization precision	43
5-2	Comparison of performance between two laser sources	44
5-3	Comparison of approaches to reject laser speckle	44
5-4	Wilcoxon rank-sum test on STORM data.	46
5-5	Wilcoxon rank-sum test on PALM data.	47

Preface

When I started this project in the summer of 2019, I had just become a father of twins. Balancing my focus on the fragile health of my two daughters and the work in the lab asked dedication, discipline and flexibility. I would like to thank Carlas for his patience with this situation and his supervision during the challenging periods of experimental work. The way to discuss practical problems I encountered during the many hours in the lab gave me many new insights and I learned a lot about optical design and experimental work in microscopy. I also want to thank Jelmer for the day to day help in the interaction between hardware and software and the daily coffee breaks during which we brainstormed. Special thanks to Taylor, who was always ready to provide expert advice. During the last couple months of this project, the coronavirus had a lot of impact on our daily lives. Thanks to all the staff who made it possible to continue working in the optical lab.

Lastly I want to thank my family and loving wife, Lilianne for her support and for giving me the opportunity to focus on this thesis project.

“To call in the statistician after the experiment is done may be no more than asking him to perform a post-mortem examination: he may be able to say what the experiment died of.”

— *Sir Robert Fisher*

Chapter 1

Introduction

The invention of the microscope was over 300 years ago and yet microscopy still is a relevant field of research. As a tool for biological and medical research, the aim to image with a higher resolution has since then increased enormously.

1-1 Fluorescence microscopy

As cells are more or less transparent, the lack of contrast in biological tissue has been a challenge for microscopists for a long time. In the second half of the 20th century, researchers were able to isolate fluorescent proteins from natural sources for the first time and express this protein in cells [2]. This spiked the interest of researchers in the field of microscopy, since this enables a high specificity and high contrast for imaging using fluorescence microscopy.

1-1-1 Fluorescence

Fluorescence is the emission of light by a molecule as a reaction to absorption of energy. This extra energy brings the fluorescent molecule into an excited vibrational state S_1^{vib} . In this state, some energy is lost in the form of vibrational movement and other processes. This brings the molecule to the excited state S_1 . From here, emission of fluorescent light occurs. Since a portion of the absorbed energy has been lost, an upward shift in wavelength occurs. This is called the Stokes-shift of a fluorophore. Figure 1-1 shows the different states of a fluorescent molecule and the shift between excitation and emission spectrum of the fluorescent molecule *Alexa* – 488.

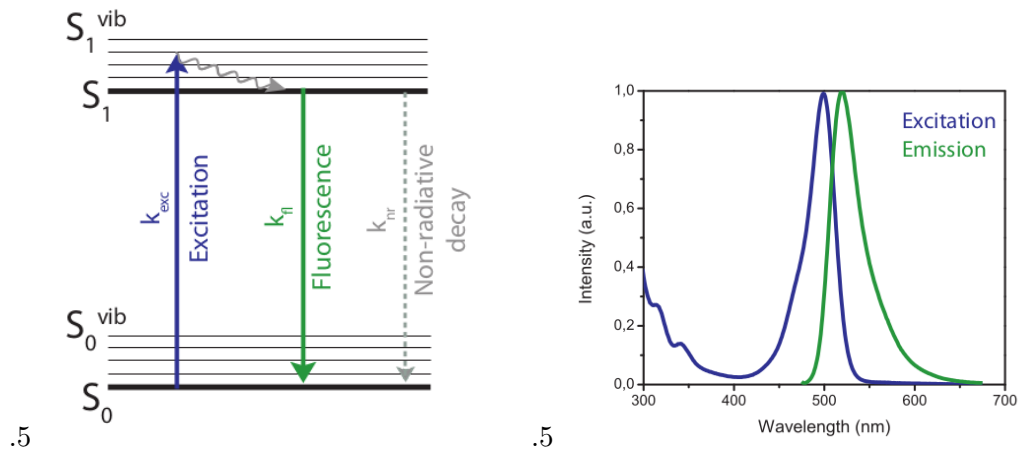


Figure 1-1: Jablonski diagram and change in wavelength of a fluorophore.

Source: Scientific Volume Imaging

1-1-2 Fluorescence in microscopy

Since fluorescent proteins can be expressed in cells, we are able to use them as fluorescent tags to biological samples. This is possible with a high specificity and results in a high contrast imaging experiment. This high contrast is achieved by decoupling the excitation and emission path of a fluorophore: as absorption of excitation light happens in a different wavelength than the emission of fluorescent light, we can separate these events using spectral filtering. The light that is projected on a fluorescent sample is decoupled from the light that is emitted using a dichroic mirror. Figure 1-2 shows an optical setup that is used for fluorescence microscopy. In this case, two lasers are led to the sample plane: a red excitation laser with light that is absorbed by the fluorescent molecule. The ultraviolet activation laser is required for photo-activatable fluorescent molecules. The red laser is reflected by the first dichroic mirror, whereas the ultraviolet laser is transmitted through the first dichroic mirror. Both laser beams are focused by the excitation lens (EL) and transmitted through the second dichroic mirror. After passing through the objective and illumination of the sample, fluorescent emission light is captured by the objective. This emission light with a shifted colour spectrum, is reflected by the dichroic mirror and focused by the tube lens, into the camera.

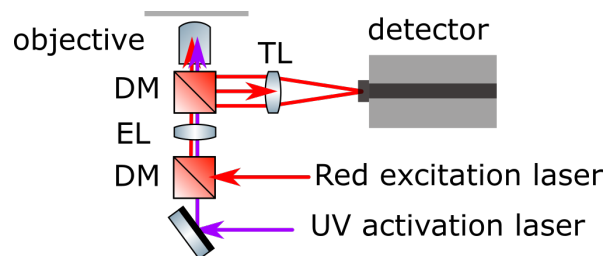


Figure 1-2: Optical setup for fluorescence microscopy. The red and ultraviolet laser are focused into the objective with the excitation lens (EL). The UV light is transmitted through both dichroic mirrors (DM), whereas the red laser is reflected by the first DM and transmits through the second DM. The emission light with the Stoke-shifted spectrum from the objective is reflected by the DM through the tube lens (TL) into the camera.

1-2 Point spread function and resolution

Image formation can be described by the convolution of the sample with the impulse response of the optical system:

$$I(x, y) = P(x, y) \cdot O(x, y) \otimes H(x, y). \quad (1-1)$$

Here, $I(x, y)$ is the measured two-dimensional image, $P(x, y)$ the (spatially varying) illumination pattern, $O(x, y)$ is the sample that is being imaged and $H(x, y)$ is the point spread function of the optical system, the two-dimensional impulse response. Because of the diffraction of light, an infinitesimal object will be mapped to the detector plane as a finite-sized spot. The microscope objective can be considered a low-pass filter to the spatial frequencies of the sample. Mathematically, we can describe the point spread function as the Fourier transform of the circular pupil plane of the objective:

$$H(x, y) = |\mathcal{F}\{P(x, y)\}|^2 = \mathcal{F}\{P(x, y)\} \cdot \mathcal{F}^*\{P(x, y)\}. \quad (1-2)$$

In 1873, the German physicist Ernst Abbe introduced the diffraction limit of light. This diffraction limit shows that the smallest observable sampling distance is bounded by the inverse of the highest spatial frequency that can be captured by the objective with Nyquist sampling:

$$d = \frac{\lambda}{2NA}. \quad (1-3)$$

Here, d is the minimum sampling distance, λ is the wavelength of light and NA is the numerical aperture of the objective, defined by $NA = n \cdot \sin \theta$. Here, n is the refractive index of the medium and θ the angle between the marginal and chief ray of the lens. Figure 1-3 shows the diffraction pattern of a circular pupil, where the fringes of the Airy function are clearly visible:

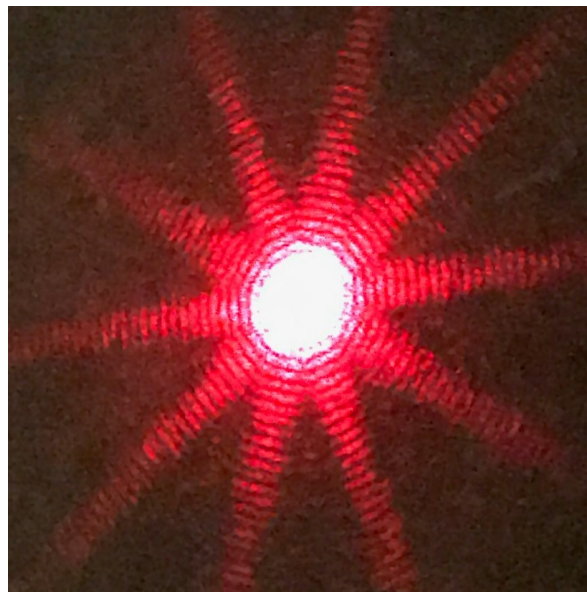


Figure 1-3: Diffraction pattern of a circular aperture. The streaks that result in a star-like shape are a result of small gaps in the adjustable iris that was used to diffract the laser beam.

A more graphical way to define the resolution is Rayleigh's resolution criterion. Rayleigh stated that two points are just resolved if the center of one Airy pattern is at the position of the first minimum of the second Airy pattern, as we show in figure 1-4:

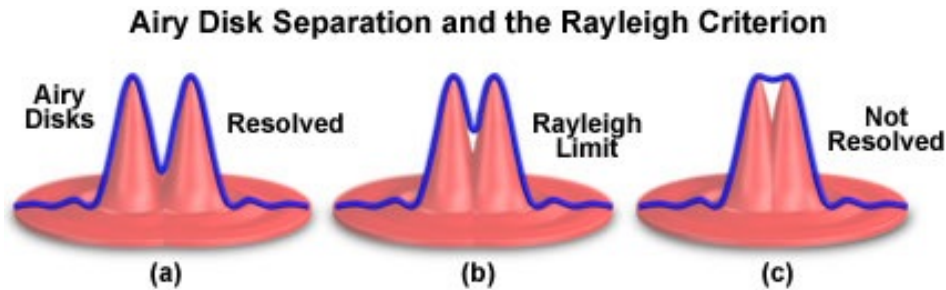


Figure 1-4: Separation of two individual PSFs. a) Two points are clearly resolved. b) The points are separated with a minimum observable distance. c) The points are too close together to distinguish them.

Source: Olympus Microscopy

Two points can only be distinguished when the distance d between them is larger than

$$d = 0.61 \frac{\lambda}{NA}. \quad (1-4)$$

1-3 Super-resolution microscopy

One way to overcome the diffraction limit is to use Single Molecule Localization Microscopy (SMLM). Two kinds are distinguished here: Stochastic Optical Reconstruction Microscopy (STORM) [3] and PhotoActivation Localization Microscopy (PALM) [4].

The way super-resolution works is by spatially and temporally separating fluorescent labels, so that each molecule is imaged as a diffraction limited spot. In direct STORM, this activation of fluorescent labels happens chemically in a stochastic way, whereas in PALM the fluorescent labels are photoactivated using a separate laser source. The resulting diffraction-limited spots can be localized with a precision far greater than the diffraction limit. The localization precision can be defined as:

$$\Delta x \approx \frac{\lambda}{NA\sqrt{N}}. \quad (1-5)$$

For an average photon count, this results in a localization precision of about $20nm$. Using the localization information of each individual spot, an image reconstruction can be performed by combining all these spots into one super-resolution image. Figure 1-5 shows the pipeline of localization microscopy.

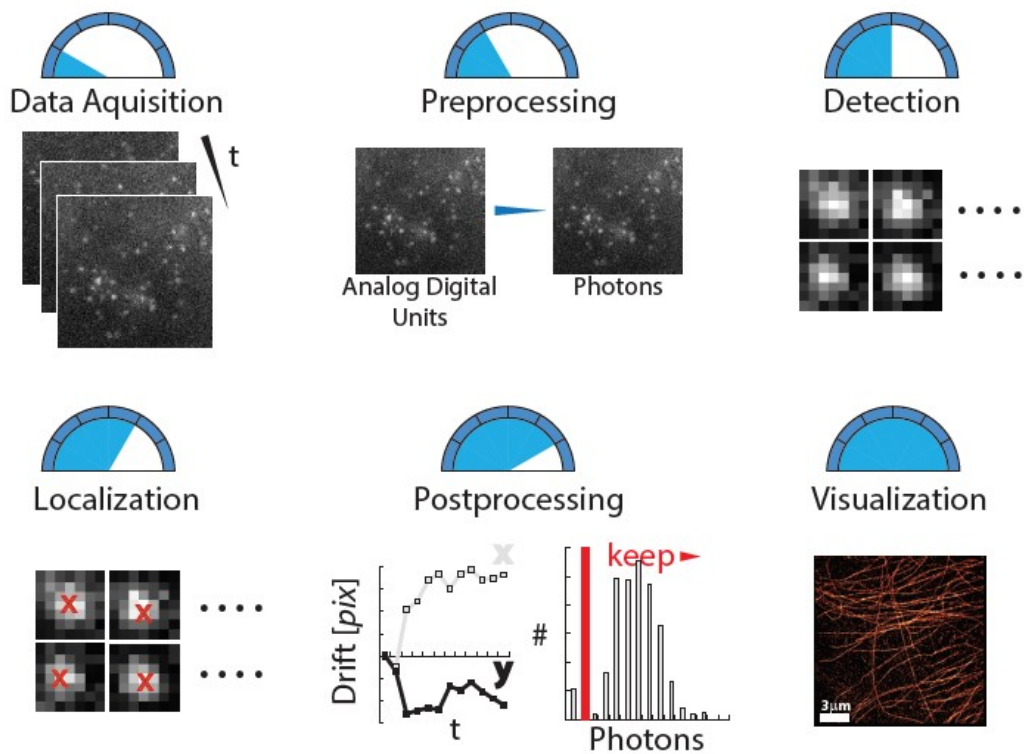


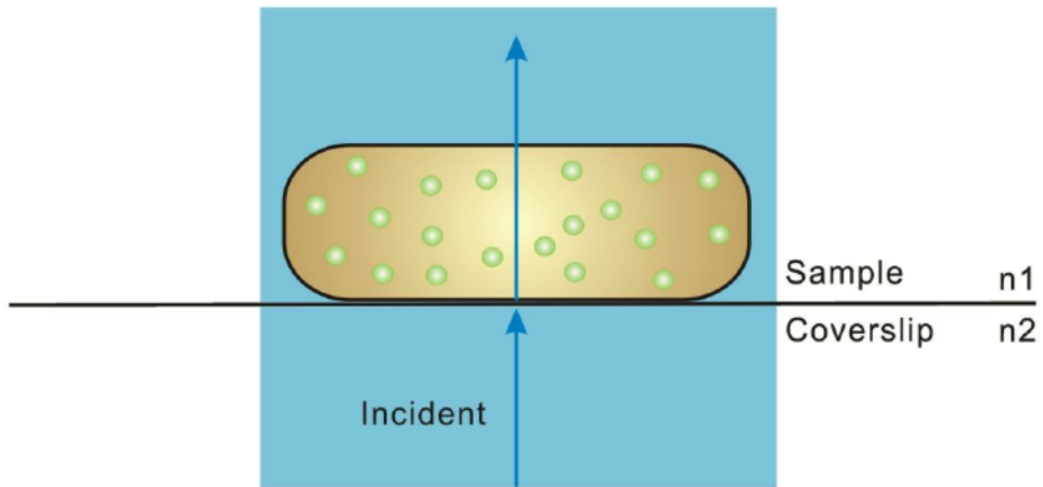
Figure 1-5: The imaging pipeline to reconstruct a super-resolution image from the raw data. 1) A series of blinking molecules is measured. 2) The raw data is converted to photon counts for each pixel. 3) Using a generalized likelihood ratio test, detection of spots is done and regions of interest are isolated [5]. 4) These spots are localized using maximum likelihood estimation. 5) Next, these localizations are corrected for drift and filtered to keep only data with realistic photon counts. 6) A reconstruction of the super-resolution image is created by combining all the emission spots and applying a Gaussian blurring filter with the Gaussian width σ kept equal to the localization precision [6].

Source: Dissertation of C.S. Smith, PhD

1-4 Total Internal Reflection Fluorescence Microscopy

A specialized way of fluorescence microscopy is total internal reflection fluorescence (TIRF). If the NA of the illumination is higher than the refractive index of the sample, total internal reflection is achieved. Next to internal reflection, an evanescent wave of excitation light is directed into the sample [7]. This yields an advantage in excitation of only fluorescent labels that are very close to the focal plane of the objective, effectively reducing out-of-focus fluorescence and therefore decreasing the amount of background light.

Epifluorescence



TIRF

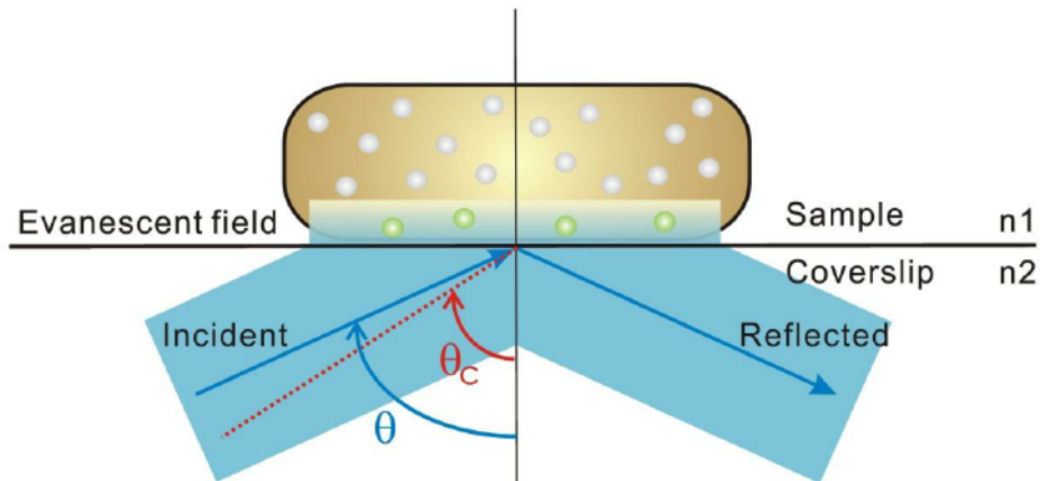


Figure 1-6: Top: In epifluorescence microscopy, the excitation beam passes through the sample, illuminating all the fluorescent molecules with excitation light. Bottom: When the incident angle θ exceeds the critical angle θ_c , an evanescent field of excitation light illuminates a small layer of the entire sample, rejecting fluorescent light from out of focus molecules.

Source:

In order to achieve total internal reflection, the incident light needs to exceed the critical angle. This is achieved by focusing the light in the back focal plane of the objective with a deviation from the optical axis. The critical angle and the NA of the objective form two bounds for the pupil plane, resulting in an annular pupil plane of width δ where the light should be focussed to contribute to TIRF imaging [8]:

$$\delta = f_b \cdot (NA - n_{sample}), \quad (1-6)$$

where f_b is the back focal length of the objective. We show this annular region in figure 1-7. Equation 1-2 shows that the PSF is related to the Fourier transform of the pupil plane. In

TIRF microscopy, only the highest spatial frequencies are used for excitation light, creating a narrower excitation PSF.

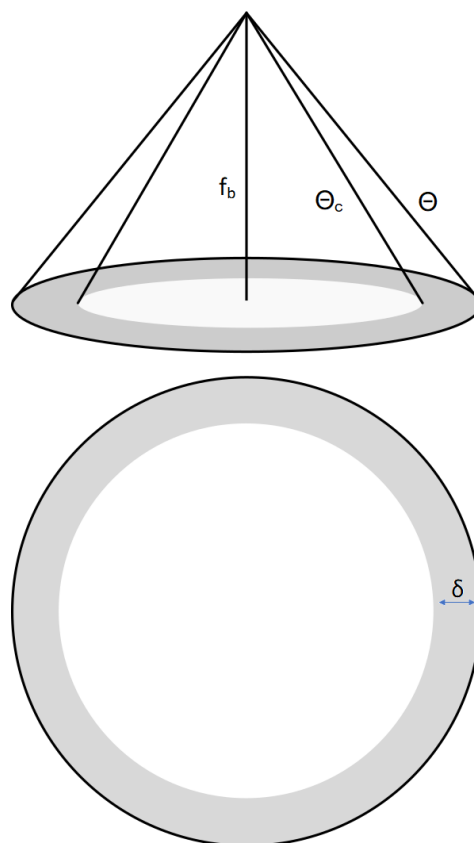


Figure 1-7: Annular region of the pupil of the objective where light can contribute to TIRF microscopy. Top: the angle θ represents the full aperture of the objective, whereas the angle θ_c represents the minimum deviation from the center of the objective. Bottom: the critical angle required for TIRF results in an annular region with width δ where light can contribute to TIRF microscopy.

1-5 Precision improvement using structured illumination light

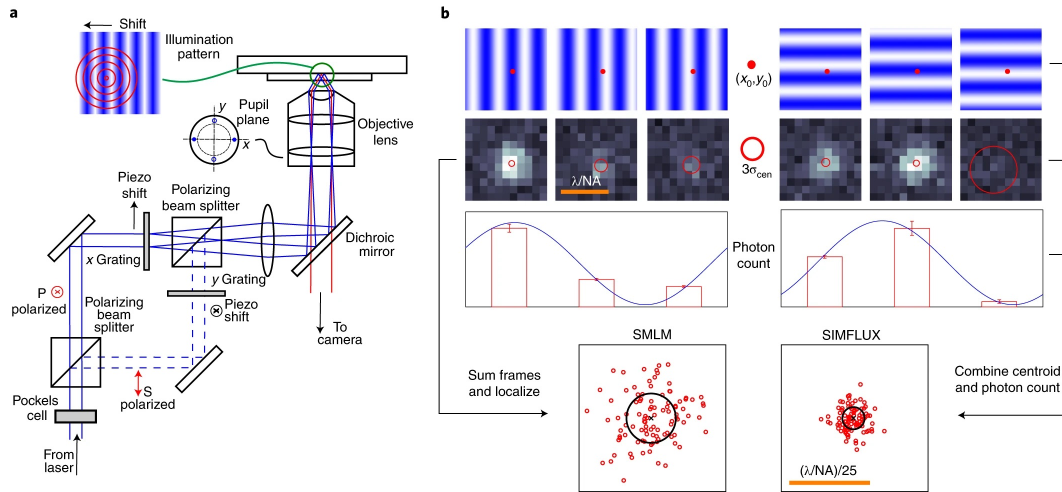


Figure 1-8: Optical setup and working principle of SIMFLUX. a) a sinusoidal illumination pattern is created in a TIRF-SIM setup as discussed in section three. b) Left: three patterns in two orthogonal directions are summed and used to create an initial estimate of the spot position like in standard SMLM with uniform illumination. Right: The additional information from the varying photon count results in a higher localization precision.

Source: Localization microscopy at doubled precision with patterned illumination [9].

Recently, a new method was developed by Cossen et al. in [9] to improve the localization precision in SMLM by introducing structured illumination. This method, called SIMFLUX, replaces the uniform excitation light of the fluorescence microscope with an illumination that varies the intensity in a sinusoidal way. A near two-fold improvement in localization precision is shown by extracting position information by pattern-induced photon count variations. We cover the relation between the structured illumination and precision improvement in section three. In SIMFLUX, a pattern is projected onto the sample plane in six different ways: two orthogonal directions and three phase steps for a full periodic cycle. By summing the photon counts of these six projections, an initial localization is done with the assumption of uniform illumination. With this information, the photon counts of all individual frames are estimated, giving rise to the estimation of the pattern pitch, phase and orientation. A new localization process is started for each individual frame, taking into account the pattern-dependent illumination intensity.

1-6 Thesis topic

When we do not have any prior knowledge on the location of a fluorescent molecule, the phase shift of each pattern is chosen to keep the localization precision as homogeneous as possible over the field of view. However, if we have a way to introduce prior knowledge on the location of a fluorescent molecule, we can choose the series of illumination patterns in such a way that we create local peaks in resolution improvement.

We present a method to create this prior knowledge on the location of photo-activatable

fluorescent molecules by selective photo-activation. Since we create local peaks in resolution improvement in a periodic way, we will also design for patterned activation. By doing this we create a high-tech system that combines highly accurate hardware with smart illumination input.

The research objective of this project is to demonstrate a precision improvement that is achieved by maximizing the information that we gain from an imaging experiment through incorporating prior knowledge. As each fluorescent molecule emits a limited amount of photons before it bleaches, we want to retrieve more information without the use of additional photons.

During this project, we design a PALM microscope using two digital micromirror devices (DMDs). In order to create a benchmark, we first build a PALM-TIRF microscope with uniform illumination. For SIMFLUX and PA-SIMFLUX, multiple phase steps are required within the on-time of a fluorophore, as is discussed in section 3-4. We use the PALM-TIRF setup to measure the on-time of the fluorescent dyes, in order to get an idea of the maximum exposure time and required frame rate. The building process of the optical setup for PA-SIMFLUX can be separated in two steps. During this project, we design a TIRF-SIM setup that enables both SIMFLUX and PA-SIMFLUX experiments. First, we recreate SIMFLUX using this DMD-setup. Next, we add the ultraviolet light path for patterned photo-activation. The design of the illumination path for the DMD-SIMFLUX setup is similar to the TIRF-SIM setup in figure 1-9.

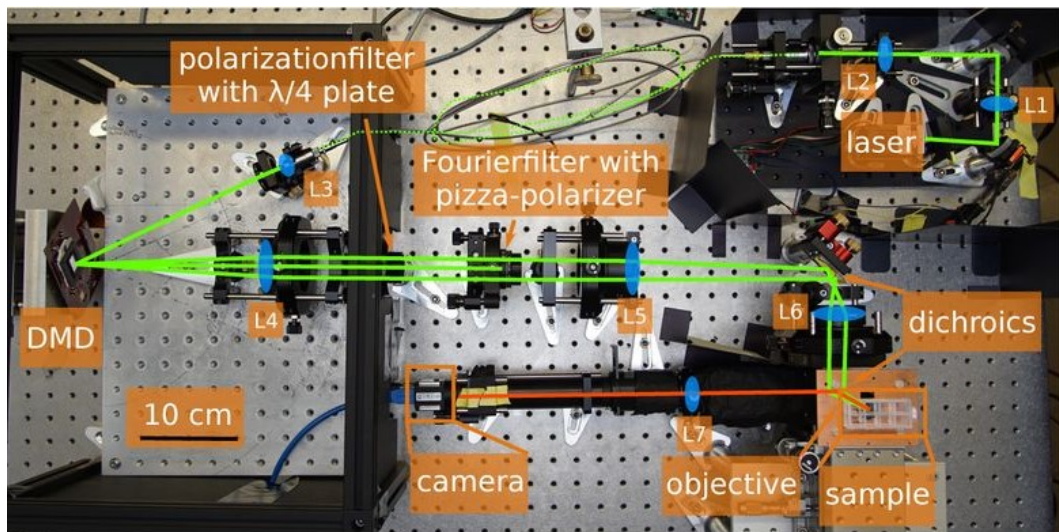


Figure 1-9: A comparable DMD-SIM setup, operating in $532nm$ light. The laser beam is expanded five times with L1 ($f = 30mm$) and L2 ($f = 150mm$), before coupled into a single-mode fiber using a $10x$ objective. The laser beam is collimated using L3 ($f = 20mm$) and incident on the DMD. L4 ($f = 200mm$) collects the diffracted light from the DMD and focuses on the Fourier plane. Here, the Fourier filter blocks the undesired diffraction orders and corrects the polarization of the light. L5 ($f = 100mm$) and L6 ($f = 150mm$) magnify the spacing of orders and focus the diffraction orders in the objective via the dichroics. Emission light from the sample plane is magnified by the objective and L7 ($f = 250mm$) focuses the light in the camera.

Source: DMD-based super-resolution structured illumination microscopy visualizes live cell dynamics at high speed and low cost [10].

Theoretical background

In this chapter, we introduce the localization of single molecule localization microscopy and its precision through the Cramer Rao Lower Bound (CRLB). We show the resolution improvement that is achieved with SIMFLUX and the expected resolution improvement through Patterned Activation-SIMFLUX. Finally, we cover the theory to simulate an optical setup using Fourier analysis.

2-1 Maximum likelihood estimation

To find the position of the diffraction-limited spots of the blinking fluorophores, Maximum Likelihood Estimation (MLE) is used to fit each isolated spot to the PSF model [11].

2-1-1 PSF model

A generic PSF model can be written as:

$$H(x, y) = I \cdot PSF(x - x_0, y - y_0) + I_{bg}. \quad (2-1)$$

Here, $PSF(x, y)$ is the PSF function on each position, x_0, y_0 are the position coordinates of the fluorescent molecule and I_{bg} is the level of background photons. A numerically efficient and valid approach for two-dimensional fitting of fluorescent molecules is the Gaussian PSF model with PSF width σ_0 [12]:

$$H_{Gauss}(x, y) = \frac{1}{2\pi\sigma_0^2} e^{-\frac{(x-x_0)^2+(y-y_0)^2}{2\sigma_0^2}}. \quad (2-2)$$

To derive the expected photon count μ at each pixel k , we integrate this function over the pixel area:

$$\mu_k(x, y) = I\Delta E_x(x_k - x_0)\Delta E_y(y_k - y_0) + I_{bg}, \quad (2-3)$$

where $\Delta E_x(x, y)$ and $\Delta E_y(x, y)$ are defined as:

$$\Delta E_x(x, y) = \frac{1}{2} \left(\frac{x_k - x_0 + \frac{1}{2}}{\sqrt{2}\sigma_0} - \frac{x_k - x_0 - \frac{1}{2}}{\sqrt{2}\sigma_0} \right), \quad (2-4)$$

$$\Delta E_y(x, y) = \frac{1}{2} \left(\frac{y_k - y_0 + \frac{1}{2}}{\sqrt{2}\sigma_0} - \frac{y_k - y_0 - \frac{1}{2}}{\sqrt{2}\sigma_0} \right). \quad (2-5)$$

Here, x_k, y_k are the pixel coordinates of pixel k . We transfer this to a maximum likelihood estimation problem, where the relation between the expected photon count μ_k and the measured pixel intensity is modelled as a Poisson distribution, under the assumption of absence of readout noise. In this optimization problem, we estimate the parameters θ_x, θ_y as the estimators for the center of the PSF x_0, y_0 and θ_I, θ_{bg} as the estimators for intensity I and background I_{bg} :

$$L(\hat{\theta}|D) = \max_{\theta} \prod_k \frac{\mu_k(\theta_x, \theta_y, \theta_I, \theta_{bg})^{d_k} e^{-\mu_k(\theta_x, \theta_y, \theta_I, \theta_{bg})}}{d_k!}. \quad (2-6)$$

Here, d_k is the measured pixel intensity and D the full set of pixels.

2-2 Fisher information and Cramer Rao Lower Bound

The maximization of the likelihood function is often done using the Levenbergh-Marquardt algorithm [13]. The precision of localization of a fluorescent spot is fundamentally limited by its photon count. A measure for the uncertainty of the estimation is the Cramer Rao Lower Bound (CRLB), which is the theoretical minimum variance for an unbiased estimator[14]. The CRLB is defined by the inverse of the Fisher information matrix:

$$Cov(\hat{\theta}) \leq I_{\hat{\theta}}^{-1}. \quad (2-7)$$

For SMLM with homogeneous illumination, the Fisher information matrix I_{θ} can be written as:

$$I_{ij}(\theta) = E \left[\sum_k \frac{(x_k - \mu_k(x, y))^2}{\mu_k(\theta_i)^2} \frac{\partial \mu_k(x, y)}{\partial \theta_i} \frac{\partial \mu_k(x, y)}{\partial \theta_j} \right]. \quad (2-8)$$

As $(x_k - \mu_k(x, y))^2$ by definition is the variance and the variance of a Poisson process is its mean, the Fisher matrix can be rewritten as:

$$I_{ij}(\theta) = \left[\sum_k \frac{1}{\mu_k(\theta_i)} \frac{\partial \mu_k(x, y)}{\partial \theta_i} \frac{\partial \mu_k(x, y)}{\partial \theta_j} \right]. \quad (2-9)$$

2-3 CRLB and patterned illumination

When illumination of the sample is non-uniform, the CRLB becomes different. This is given in the supplementary notes of the SIMFLUX paper [9]:

Numerical localization precision For the illumination of the sample, $j = 1, 2, \dots, J$ harmonic illuminations are present with $l = x, y$ orientations as a function of pattern phase ϕ :

$$\sum_{l=1}^L \sum_{j=1}^J P(\phi_{lj}(x, y)) = 1. \quad (2-10)$$

The phase is defined by the cross product of the spatial frequency vector \vec{q}_l and the spatial coordinate vector $\vec{r} = \begin{bmatrix} x \\ y \end{bmatrix}$:

$$\phi_{lj}(x, y) = 2\pi \vec{q}_l \cdot \vec{r} - \psi_{lj}. \quad (2-11)$$

We can define the spatial frequency vector by:

$$\vec{q}_l = \frac{1}{p}(\cos \beta_l, \sin \beta_l), \quad (2-12)$$

where $\beta_l = \frac{\pi l}{L} + \beta_0$, with β_0 a global angular offset. With this, the illumination pattern is defined. The PSF model that is used is the Gaussian model, introduced in equation 2-2. The expected fluorescence photon count for each pixel j will depend on the illumination intensity $P(\phi_{lj})$:

$$\mu_k^{lj} = I \cdot P(\phi_{lj}(x_0, y_0)) \Delta E_x(x_k - x_0) \Delta E_y(y_k - y_0) + \frac{b}{LJ}. \quad (2-13)$$

Here, the total background is divided by the total number of pattern projections. With a sinusoidal illumination pattern like in SIMFLUX, $P(\phi)$ can be described as:

$$P(\phi) = \frac{1}{LJ}(1 + m \cos \phi). \quad (2-14)$$

When the phase steps between each illumination pattern is assumed to be equidistant, the phase is defined as follows:

$$\psi_{lk} = 2\pi(k-1)/J + \chi_l, \quad (2-15)$$

with χ_l the the phase offset in pattern direction l . The expected pixel intensity, when taking into account a finite pixel size and a constant background, is defined as:

The resolution can be derived numerically and depends on the number of phase steps in each period 2π . When the amount of equidistant phase steps is increased, the overall precision is more homogeneous, but the CRLB has a higher mean. We will show this in figure 3-1 and 3-2 through a simulation of the localization precision.

2-4 Fourier optics

We already introduced the point spread function as the Fourier transform of the pupil function. We can apply this theory further to model the optical system by using Fourier analysis. In this section we cover the use of Fourier optics to model the optical behaviour. We do this by applying the work of J. Goodman's Introduction to Fourier optics [15].

2-4-1 Propagation and diffraction

Propagation of light waves

We use the Helmholtz equation to model the wave propagation:

$$\nabla^2 U(\vec{r}) + k^2 U(\vec{r}) = 0 \quad (2-16)$$

with $k = \frac{2\pi}{\lambda}$ and $U(\vec{r})$ the wavefield for a given position in space. This results in the general solution:

$$U(\vec{r}) = \int d^3 f \hat{U}(\vec{f}) e^{2\pi j \vec{f} \cdot \vec{r}}. \quad (2-17)$$

Here, $\vec{f} = \sqrt{f_x^2 + f_y^2 + f_z^2} = \frac{1}{\lambda}$. By substituting $f_z = \pm \sqrt{\frac{1}{\lambda^2} - (f_x^2 + f_y^2)}$, we get the equation for backward and forward propagation of a wave. If we separate this, we can describe forward propagation as:

$$\hat{U}(f_x, f_y, z_+) = \hat{U}_+(f_x, f_y) e^{2\pi j f_z z}, \quad (2-18)$$

where $f_x^2 + f_y^2 \leq \frac{1}{\lambda^2}$. We can connect the spatial frequencies to the spatial coordinates using figure 2-1 and the following transformations:

$$f_x = \frac{\sin \theta \cos \phi}{\lambda} \quad (2-19)$$

$$f_y = \frac{\sin \theta \sin \phi}{\lambda} \quad (2-20)$$

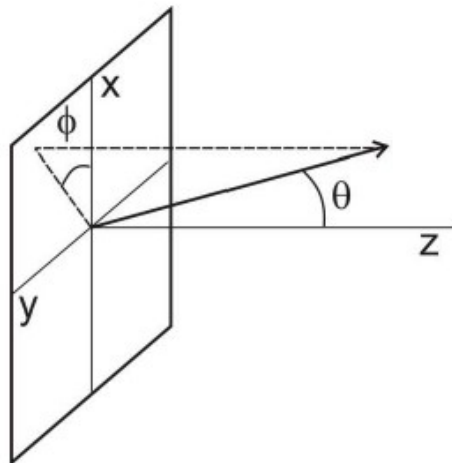


Figure 2-1: Schematic overview of the optical planes. Here, x, y is the optical plane, z is the optical axis. ϕ and θ are the radial and azimuthal angles.

Source: Imaging Systems, lecture notes

Diffraction theory

Diffraction happens if a propagating light wave encounters an aperture. Numerically, this can be modelled efficiently by Fourier theory. The wavefield at a distance z after the aperture can be defined as:

$$U(x, y, z) = \frac{U_0(x, y, z)e^{\frac{2\pi jz}{\lambda}}}{j\lambda z} \hat{T}(f_x, f_y), \quad (2-21)$$

where $f_x, f_y = \frac{x}{\lambda z}, \frac{y}{\lambda z}$. The most common example is the circular aperture, resulting in an Airy disk pattern as shown before in figure 1-3.

2-4-2 Lens as a Fourier Transformer

When a wavefield of light interacts with a lens, phase change occurs. This phase change is described as:

$$\Delta\phi = \frac{\pi(x^2 + y^2)}{\lambda F}, \quad (2-22)$$

where F is the focal length of the lens. This results in a change of wavefield:

$$U_{out}(x, y) = e^{\frac{-\pi j(x^2 + y^2)}{\lambda F}} U_{in}(x, y). \quad (2-23)$$

When we apply this for the distance from back focal plane to front focal plane, we end up with:

$$U_{front}(x, y) = \frac{e^{4\pi jF}}{j\lambda F} \hat{U}_{back}\left(\frac{x}{\lambda F}, \frac{y}{\lambda F}\right) \quad (2-24)$$

2-4-3 Telescope system

An often used subsystem in optics is a two-lens system, where the back focal plane of the second lens is aligned with the front focal plane of the first lens. This results in a system with four focal lengths (4f-system). Combining equation 2-24 for each lens and neglecting a constant scaling factor gives:

$$U_{im}(x_2, y_2) = \int \int dx dy P(x, y) \exp -\frac{2\pi j(x_2x + y_2y)}{\lambda F_2} \otimes U_{obj}(x_1, y_1). \quad (2-25)$$

In this equation, the new coordinates x_2, y_2 are defined by $x_2 = \frac{F_2}{F_1}x_1, y_2 = \frac{F_2}{F_1}y_1$.

2-4-4 High NA focusing

For lenses with an $NA < 1$, scalar theory on focusing can be used. However, for lenses with higher NA , such as most objectives, this is no longer possible. For these cases, we need to take into account the vectorial effects. For this, we consider the three dimensional incoming electric field vector:

$$\begin{bmatrix} E_x^{in} \\ E_y^{in} \\ E_z^{in} \end{bmatrix} \quad (2-26)$$

Figure 2-2 shows the change in direction of each vector.

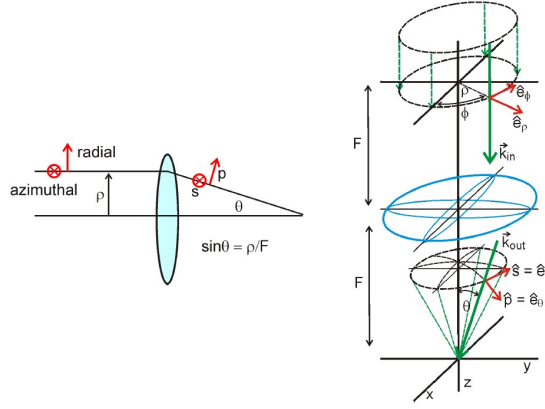


Figure 2-2: The change in direction of vectorial components is caused by the high NA focusing of a lens.

To properly cope with this direction in change, a coordinate change is presented from Cartesian to cylindrical coordinates using matrix $R(\hat{e}_z, -\phi)$:

$$\begin{bmatrix} E_\rho^{in} \\ E_\phi^{in} \\ E_z^{in} \end{bmatrix} = \begin{bmatrix} \cos \phi & \sin \phi & 0 \\ -\sin \phi & \cos \phi & 0 \\ 0 & 0 & 1 \end{bmatrix} \begin{bmatrix} E_x^{in} \\ E_y^{in} \\ E_z^{in} \end{bmatrix}. \quad (2-27)$$

Next, the outgoing spherical coordinates, need to be rotated around \hat{e}_ϕ with angle θ to transform back to cylindrical coordinates with matrix $R(\hat{e}_\phi, \theta)$:

$$\begin{bmatrix} E_\rho^{out} \\ E_\phi^{out} \\ E_z^{out} \end{bmatrix} = \begin{bmatrix} \cos \theta & 0 & \sin \theta \\ 0 & 1 & 0 \\ \sin \theta & 0 & \cos \theta \end{bmatrix} \begin{bmatrix} E_\theta^{out} \\ E_\phi^{out} \\ E_\rho^{out} \end{bmatrix}. \quad (2-28)$$

Additionally, the back transformation is also formed, to transform the cylindrical coordinates back to Cartesian with the rotational matrix $R(\hat{e}_z, \phi)$:

$$\begin{bmatrix} E_x^{out} \\ E_y^{out} \\ E_z^{out} \end{bmatrix} = \begin{bmatrix} \cos \phi & \sin \phi & 0 \\ -\sin \phi & \cos \phi & 0 \\ 0 & 0 & 1 \end{bmatrix} \begin{bmatrix} E_\rho^{out} \\ E_\phi^{out} \\ E_z^{out} \end{bmatrix}. \quad (2-29)$$

Combining these matrices, we can establish the total coordinate change by the lens matrix M_{lm} :

$$\begin{bmatrix} E_x^{out} \\ E_y^{out} \\ E_z^{out} \end{bmatrix} = \begin{bmatrix} \cos \theta \cos^2 \phi + \sin^2 \phi & (\cos \theta - 1) \sin \phi \cos \phi & -\sin \theta \cos \phi \\ (\cos \theta - 1) \sin \phi \cos \phi & \cos^2 \phi + \cos \theta \sin^2 \phi & -\sin \theta \sin \phi \\ \sin \theta \cos \phi & \sin \theta \sin \phi & \cos \theta \end{bmatrix} \begin{bmatrix} E_x^{in} \\ E_y^{in} \\ E_z^{in} \end{bmatrix}. \quad (2-30)$$

Next, we can again apply the lens equation as a Fourier transformer:

$$E_{\text{front},l}(\vec{r}') = \frac{1}{j\lambda F} \iint d^2r A(\vec{r}) \sum_{m=x,y,z} M_{lm}(\vec{r}) E_{\text{back},m}(\vec{r}) e^{-\frac{2\pi j \vec{r}' \cdot \vec{r}}{\lambda F}}, \quad (2-31)$$

for $l = x, y, z$. Here r' are the scaled coordinates.

2-5 Polarization of light

The polarization of light depends on the phase difference between vectorial components of the wavefield:

$$\vec{U} = \begin{bmatrix} U_x \\ U_y \end{bmatrix} \quad (2-32)$$

When the phase difference between the x- and y-component is 0 and the amplitudes are equal, the polarization is linear. By introducing a phase delay, the polarization is changed. This delay can be calculated by applying matrix algebra to the wavefield vector

$$\vec{U}' = L\vec{U}, \quad (2-33)$$

where L is the Jones matrix causing a polarization change. Two cases can be distinguished: the quarter-wave plate (QWP) and the half-wave plate (HWP). The respective Jones matrices are:

$$L(\text{QWP}) = \begin{bmatrix} 1 & 0 \\ 0 & -j \end{bmatrix} \quad (2-34)$$

$$L(\text{HWP}) = \begin{bmatrix} 1 & 0 \\ 0 & -1 \end{bmatrix} \quad (2-35)$$

A quarter-wave plate changes the linearly polarized state into a circular polarization state and the other way around, while a half-wave plate changes with a linearly polarized input light will only change the orientation of the linearly polarized light.

2-5-1 Measuring the polarization state

To assess the polarization state, a linear polarizer (LP) with a high extinction ratio should be used. An economic option is the wiregrid polarizer by Thorlabs (WP25M-VIS). We can conclude on the polarization state by measuring the power behind the LP as a function of the orientation angle of the LP. When the light is circularly polarized, the intensity of the transmitted light does not depend on the orientation of the LP. We show this by applying the Jones matrix $L(\alpha)$ of a LP to the circularly polarized wavefield \vec{U}_{in} , with α the orientation of the LP:

$$\vec{U}_{out}(\alpha) = L(\alpha)\vec{U}_{in} = \begin{bmatrix} \cos^2 \alpha & \sin \alpha \cos \alpha \\ \sin \alpha \cos \alpha & \sin^2 \alpha \end{bmatrix} \frac{1}{\sqrt{2}} \begin{bmatrix} 1 \\ -j \end{bmatrix} \quad (2-36)$$

$$U_{out}(\alpha) = \frac{1}{\sqrt{2}} \begin{bmatrix} \cos^2 \alpha - j \sin \alpha \cos \alpha \\ \sin \alpha \cos \alpha - j \sin^2 \alpha \end{bmatrix} \quad (2-37)$$

The measured intensity is equal to:

$$I_{out} = \vec{U}_{out}^* \vec{U}_{out} \quad (2-38)$$

$$= \frac{1}{2} \begin{bmatrix} \cos^2 \alpha + j \sin \alpha \cos \alpha & \sin \alpha \cos \alpha + j \sin^2 \alpha \end{bmatrix} \begin{bmatrix} \cos^2 \alpha - j \sin \alpha \cos \alpha \\ \sin \alpha \cos \alpha - j \sin^2 \alpha \end{bmatrix} \quad (2-39)$$

$$= \frac{1}{2} (\cos^4 \alpha + \sin^4 \alpha + 2 \sin^2 \alpha \cos^2 \alpha) = \frac{1}{2} (\cos^2 \alpha + \sin^2 \alpha)^2 = \frac{1}{2}, \quad (2-40)$$

a constant value independent of the orientation angle α . However, when the light is purely linear, we expect a high modulation between maximum power and zero intensity that depends on the orientation of the LP. This modulation deteriorates if the polarization state of the light is elliptical.

2-6 Digital Micromirror Devices

As we mentioned before, we use Digital Micromirror Devices (DMDs) to create the desired patterns. A DMD is a micro-opto-electromechanical system (MOEMS). It consists of an array of micromirrors that can be independently controlled in a binary way. This results in an 'ON' and 'OFF' state for each micromirror, resulting in reflection in either +12 or -12 degrees from the neutral position.

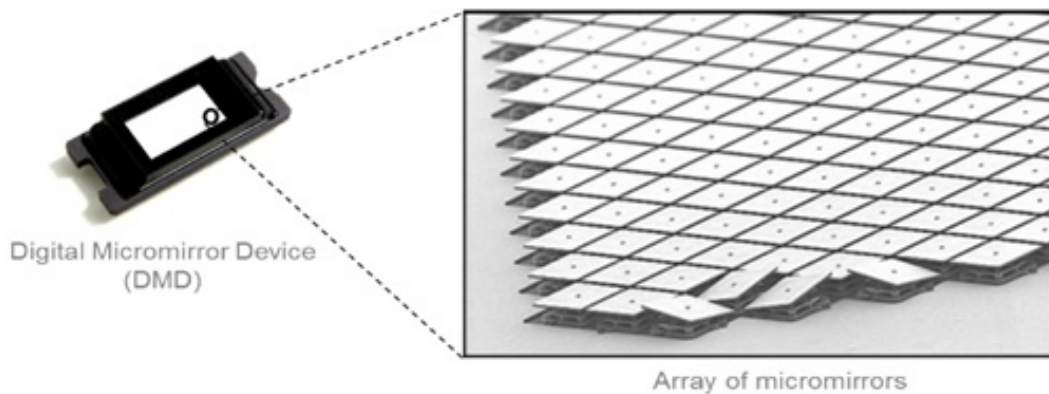


Figure 2-3: A DMD consists of individually controlled micromirrors.
Source: Texas Instruments

In the 'ON' state, laser light is reflected into the optical path, whereas in the 'OFF' state, the light is directed to a heat sink. By individually controlling each micromirror like an image pixel, a pattern can be projected into the optical path.

A large advantage of the DMD is that it can change patterns in the order of kHz. This enables the design of fast DMD-SIM setups. When DMDs are illuminated with a coherent light source, their behaviour can be described as a blazed grating. Figure 2-4 shows this configuration, where all DMD pixels are "ON":

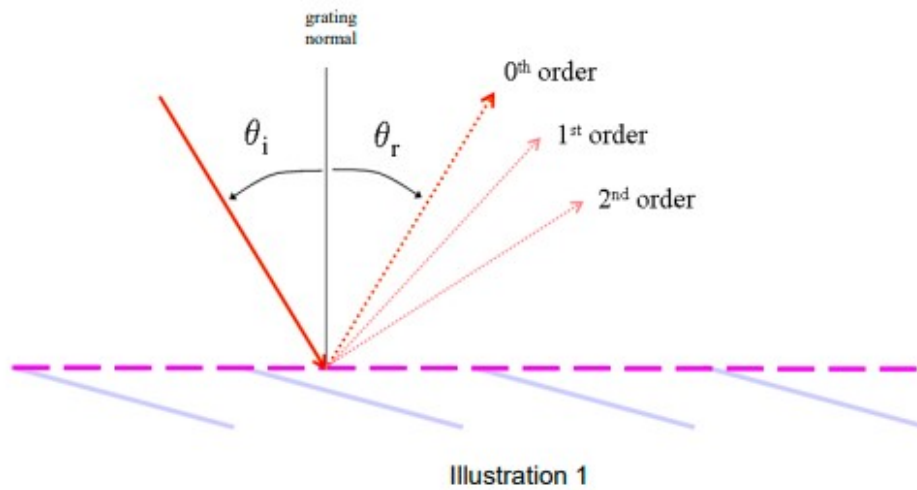


Figure 2-4: When all the pixels of the DMD are turned in the "ON" state, a blazed grating configuration is created. θ_i is the incident angle of the grating and θ_r is the reflection angle of the grating. When the blaze condition is fulfilled, this reflection angle aligns with the 0th order.

Source: Using lasers with DLP^o technology by Texas Instruments

This blazed grating effect is covered in the work of Sandmeyer et al. [10]. Since the DMD mirrors tilt along their diagonal axis, the DMD is rotated 45 degrees so that both the incident light beam and the reflected light beam can be parallel to the optical table surface. The goal here is to define the blaze angle for incident light. If we can fulfill the blaze condition by finding the correct incident angle, the diffraction envelope of the DMD aligns perfectly with the zero order reflection. The incident angle is found where the pairs of first diffraction orders have an intensity that is most equal. When this happens, the grating equation defines the angle θ for each diffraction order m :

$$\sin \theta_m = m \frac{\lambda}{p}. \quad (2-41)$$

Here, θ is the angle between the grating normal and the diffraction order, m is the integer number for the m^{th} diffraction order, and p the pitch of the grating.

Chapter 3

Simulations and optical design

Here we discuss the simulations on improving the localization precision, like we discussed in section two. Furthermore, we present the design of the experimental TIRF-SIM setup using two DMDs.

3-1 Precision improvement with structured illumination

We present the precision improvement through structured illumination using simulations of the CRLB. For these simulations, we use a photon count of 1000 and a background level of 10 photons. The emission and background photons are divided by the total number of patterns. The pitch of the pattern in this simulation is 218nm like in SIMFLUX and the modulation depth is ideal. The phase steps are chosen to be equally divided over the pattern pitch. This results in a total excitation of 1, independent of the location. The CRLB is derived and compared to the case of uniform illumination. We plot the improvement factor for each position over the length of the pattern period.

As we increase the number of phase steps from two to three, the resolution becomes more homogeneous. If we want to increase the number of phase steps, the size of the phase step will have to decrease accordingly.

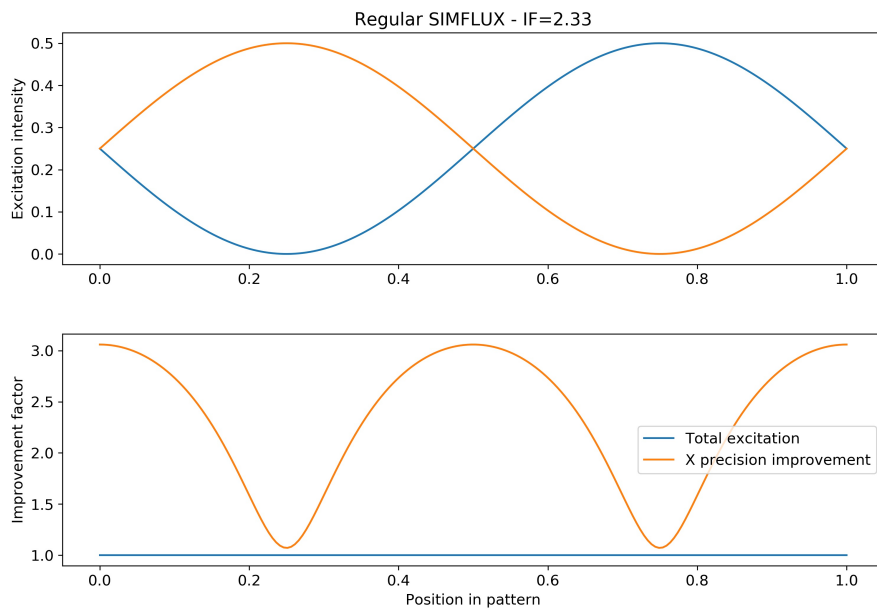


Figure 3-1: Precision improvement with two phase steps in SIMFLUX. Top: two illumination patterns, shifted in phase exactly half a period. Bottom: the total illumination intensity is constant over the field of view. The precision improvement depends heavily on the position in the field of view.

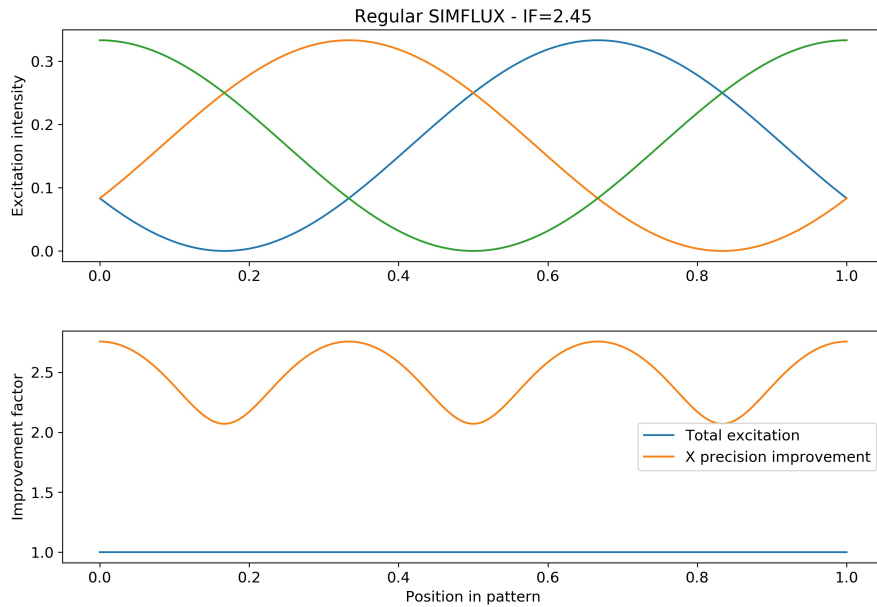


Figure 3-2: Precision improvement with three phase steps in SIMFLUX. Top: three illumination pattern, shifted in phase exactly one third of a period. Bottom: the total illumination intensity is constant over the field of view. The precision improvement becomes more homogeneous by increasing the number of phase steps from two to three.

3-2 Increased precision improvement with patterned activation

If the phase steps between illumination patterns are not equidistant in subsequent frames, the result is a highly variant resolution over the field of view, related to the pattern. In patterned activation SIMFLUX, the non-homogeneous resolution improvement is exploited by selective activation of fluorescent labels in the high resolution regions. This is possible for PALM, as an additional activation laser is used to photo-activate fluorescent markers. We show this in figure 3-3. Here, we simulate again with 1000 photons for an emission spot and 10 background photons. Instead of uniform photoactivation, we selectively activate the region where the precision improvement is maximal. The improvement factor in each location is scaled with the probability of photoactivation on this location to derive the mean improvement factor.

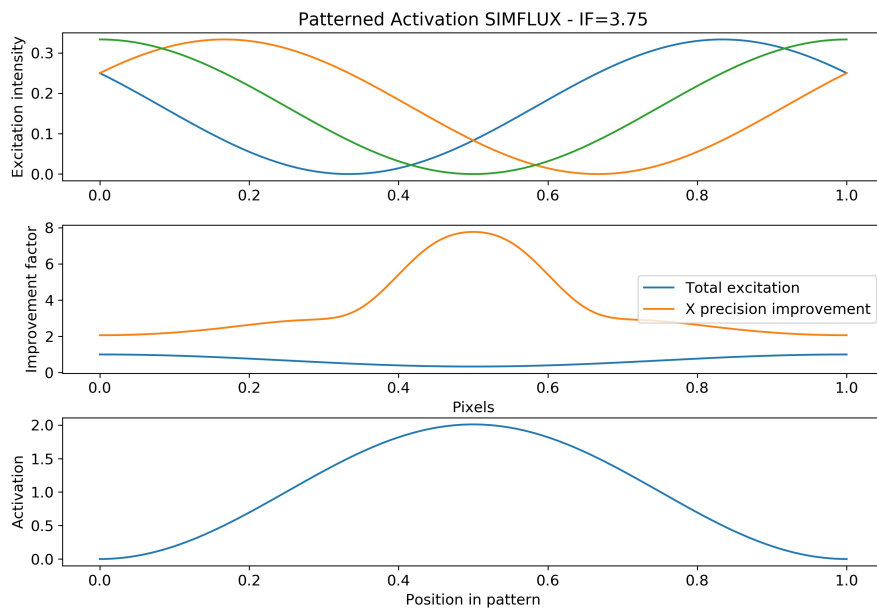


Figure 3-3: Localization precision with three non-equal phase steps in structured illumination. Top: Instead of one third of a wavelength, the three illumination patterns are one sixth of a wavelength apart. Middle: this creates a local region with a high precision improvement and a summed excitation intensity that is not constant. Bottom: using Patterned Activation, we selectively activate this region for fluorescence emission.

We show this in figure 3-4, where the patterned activation is shown to achieve high resolution locally.

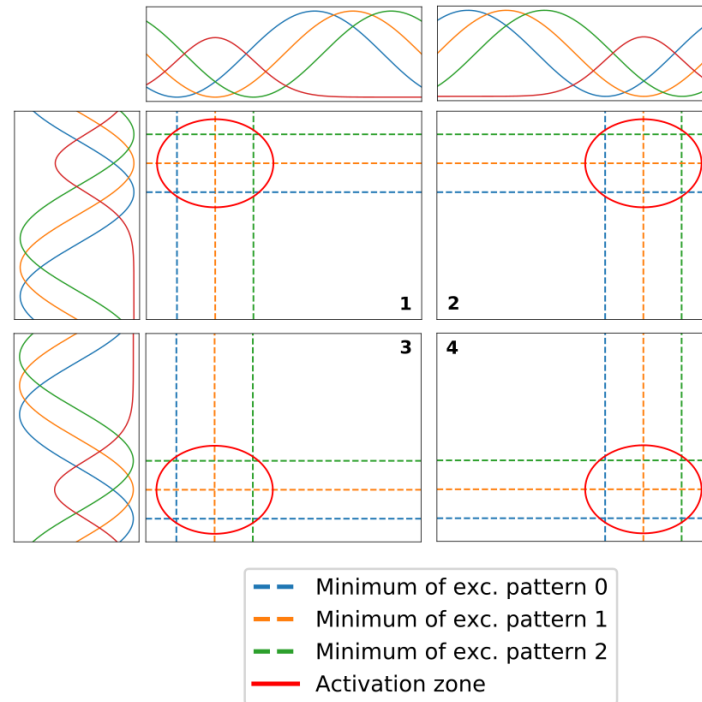


Figure 3-4: Overview of selective activation in the regions where locally high resolution is achieved by non-homogeneous patterned illumination. Since the illumination of the sample happens in a periodic way, the photoactivation is matched with a recurring activation laser spot. The illumination patterns are shown in blue, orange and green. The activation laser is shown in red.

3-3 Design of the optical setup

In order to create structured illumination on the sample plane, we design a TIRF-SIM microscope setup. Structured Illumination Microscopy uses two interfering beams to create a sinusoidal pattern on the sample plane. In order to achieve TIRF imaging, the NA of these interfering illumination beams need to exceed the refractive index of the sample. In this project, we use a 640nm single mode excitation laser from Toptica for the illumination path. We use an Olympus TIRF objective lens with an NA of 1.49, combined with a tube lens of 180mm. The diffraction limit of the objective for the excitation light is 214.76nm, using equation 1-3. To achieve TIRF imaging, the illumination NA should be larger than 1.35, resulting in a pattern pitch that is limited at 237nm. We design a setup with a pattern pitch of 231nm, which corresponds to an illumination NA of 1.39: the diffraction peaks to create this pattern have a distance of 4.17mm from the optical axis and the focal length of the objective is 3 mm. This leads to:

$$NA_{ill} = \frac{4.17}{3} = 1.39. \quad (3-1)$$

For photo-activation, we use a 405nm single mode laser from Toptica. The design of PA-SIMFLUX requires a matching pitch of the photoactivation laser. Due to design constraints, the optical path of the photoactivation laser results in a pitch of 233nm.

3-3-1 Illumination light path

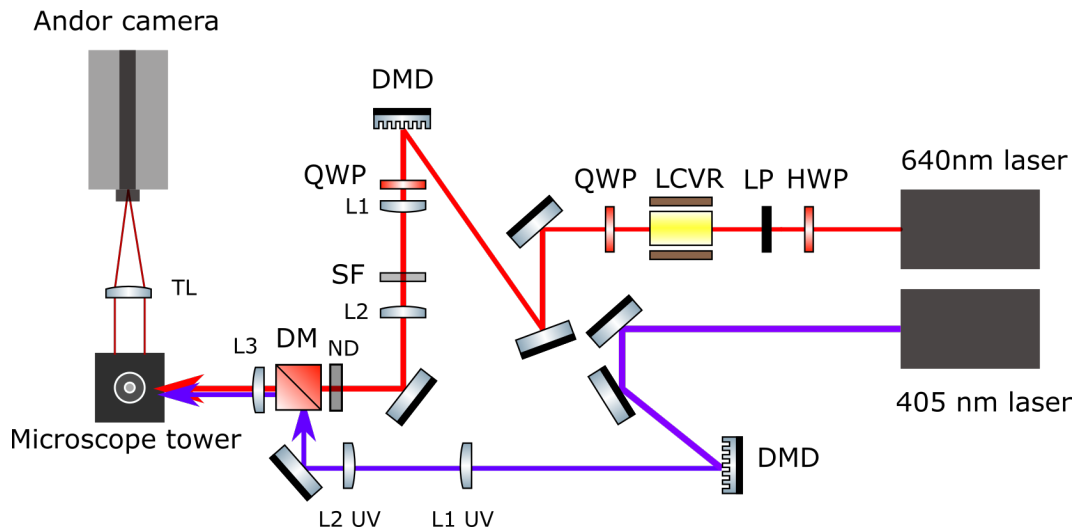


Figure 3-5: Optical design of the DMD setup. The 640nm laser points the light beam through the halfwaveplate (HWP), through the linear polarizer (LP) into the liquid crystal variable retarder (LCVR) and through the quarterwaveplate (QWP). From here, the light is directed using mirrors into the DMD. Using lenses L1, L2 and L3, the light is focused in the microscope objective tower. The neutral density (ND) filter ensures equal intensity of all diffraction peaks. The photoactivation path is directed through $L1_{UV}(f = 125mm)$ and $L2_{UV}(f = 30mm)$ into the excitation light path using the dichroic mirror (DM).

To create the structured illumination on the sample plane, we designed the optical setup that we show in figure 3-5. The DMD that we use is a Vialux V-7000 with a pixel pitch of $13,7\mu m$. The DMD projects the required patterns to induce the diffraction. We show an overview of the described planes in figure 3-6.

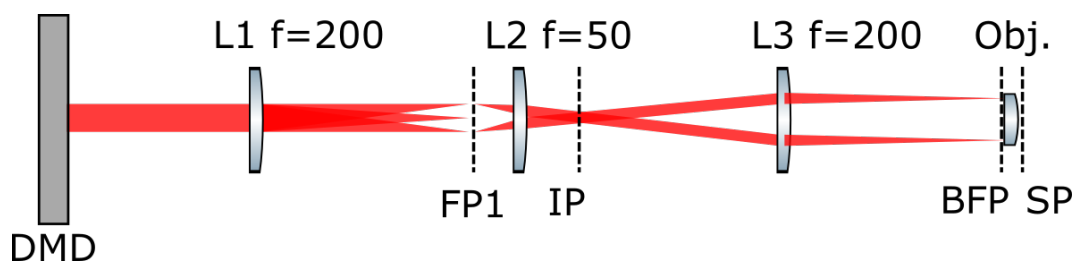


Figure 3-6: Different planes of the excitation path through the setup. First, the DMD reflects the pattern into lens L1. The diffraction orders in Fourier plane 1 (FP1) are spatially filtered, so that only the first diffraction orders are transmitted. Lens 2 and lens 3 map these diffraction orders to the back focal plane (BFP), to the desired distance from the optical axis.

The diffracted light is focused by the lens $L1$, with a focal length of 200mm. Figure 3-7 shows the projected square wave on the DMD plane and the resulting diffraction in the intermediate Fourier plane FP1. We use equation 2-24 to define the field in FP1 and plot the intensity of this field.

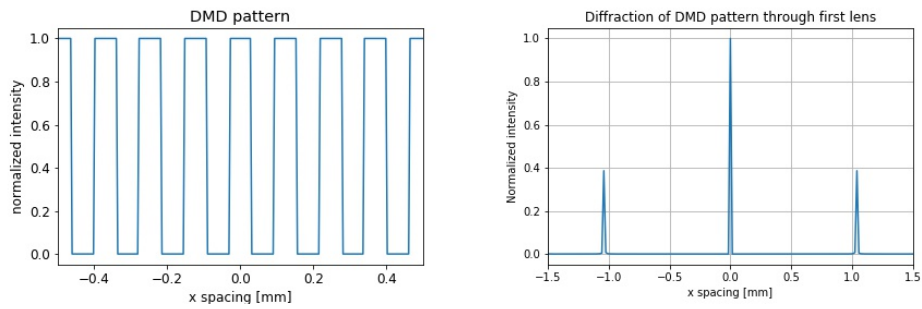


Figure 3-7: Diffraction from the projected square wave on the DMD to the intermediate plane. Left: the DMD reflects a square wave pattern into the optical light path. Right: lens L1 collects this diffraction into multiple orders, of which the zero order and the first orders are passed through the limited diameter of the lens.

We design a custom spatial filter (SF) to block out the center frequencies and unwanted higher frequencies. This is a laser-cut sheet of aluminium that can be fit in a pinhole mount. This results in a cleaned intermediate Fourier plane, like we show in figure 3-8:

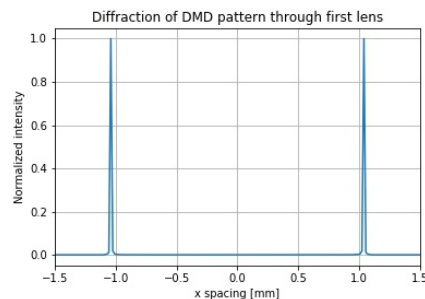


Figure 3-8: Normalized diffraction pattern in the Fourier plane of lens 1. Here, the center peak of the zero order diffraction is filtered out by the spatial filter that is placed exactly on the Fourier plane.

We use a telescope system of lenses L2 ($f=50\text{mm}$) and L3 ($f=200\text{mm}$) to create the desired magnification between the intermediate plane (FP1) and the back focal plane of the objective. The resulting field is calculated by using equation 2-25. The intensity of the resulting wave field gives the following back focal plane (BFP) image:

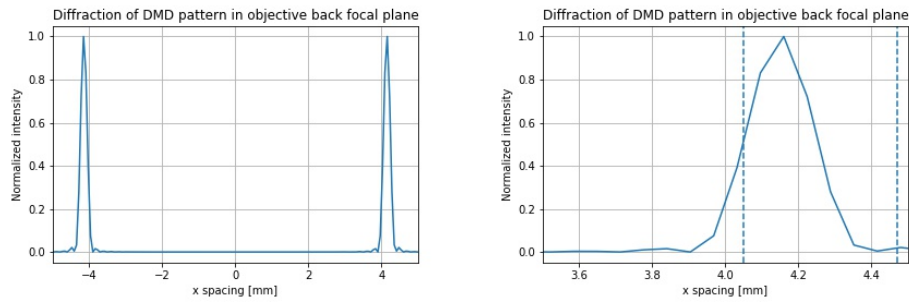


Figure 3-9: Normalized intensity profile of the back focal plane. Left: the two diffraction peaks that are mapped from the intermediate Fourier plane (FP1) onto the back focal plane of the objective. Right: a zoom in of the location of the peak in the back focal plane. The dashed lines form the lower and upper limit of the illumination NA for TIRF microscopy. Due to the spreading of the diffraction peaks, a small portion of the light of about 10 % contributes to non-TIRF microscopy

The two peaks in the back focal plane create an interference in the sample plane of the objective. To calculate this, we use equation 2-31 for high NA focusing. We show the intensity profile of the resulting wavefield in figure 3-10:

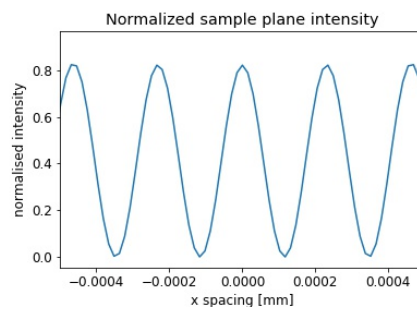


Figure 3-10: The sinusoidal signal on the sample plane of the objective. The period of the signal is 231nm and the modulation contrast is ideal in the simulated scenario, although the maximum of the intensity varies over the field due to numerical limitations.

3-3-2 Photo-activation light path

For the patterned activation, we design a second light path for the UV-laser. For this light path, the DMD that we use is a Vialux V-9601 with a pixel pitch of $10,8\mu\text{m}$. For this system, the excitation lens is shared and therefore a design constraint. The goal is to match the pattern pitch of the illumination path. This is achieved by adding a telescope system with a 30mm and a 125mm lens between the excitation lens and the DMD, like we have previously shown in figure 3-5.

3-4 Alignment of the system

The optical system consists of a couple of components with varying degrees of freedom. First, we place the microscope tower onto the optical table, as this element has no degrees of freedom. The microscope tower houses the excitation filter, the dichroic mirror and the objective lens, as well as a mirror to reflect the emission light towards the camera.

Secondly, we place a mirror to direct the optical path into the microscope tower. This is done by placing a temporary mirror that replaces the DMD. When the optical path is aligned so that a collimated light beam exits the microscope tower, we place the excitation lens and objective lens. The excitation lens is moved linearly and axially so that the beam exiting the microscope is collimated and aligns with the optical path. After we position the excitation lens, we remove the microscope objective and place the 50mm lens. We evaluate the focal position by using a shearplate interferometer to ensure the collimation of the outgoing beam. We correct the position of the lens by making sure the light path does not deviate from the optical path. When the correct position of the excitation lens is found, we create a two lens system using the 50mm lens and the 200mm lens by temporarily removing the 200mm excitation lens from the setup. Again, we ensure the position for the lens so that a collimated beam exits this 4f-system and no deviations are introduced from the optical path.

The next step is to place the DMD in the focal plane of the 200mm lens. We do this by using the objective mount to place a collimated laser source and focus the light using the 200mm lens. The position of focus is the desired DMD position. Finally, we redirect the laser into the DMD with the correct incident angle.

3-5 Polarization control

The performance of a TIRF-SIM microscope depends highly on the modulation depth of the patterned illumination light. The polarization of the light has a large impact on the modulation depth. The two interfering beams need to be equal in amplitude, as well as in polarization [10, 16, 17]. The influence of polarization on the modulation contrast of a SIM pattern is shown by O'Holleran et al. in [16] and Hsiao-Chih Huang et al. in [17]. Figure 3-11 shows the relation between polarization alignment and modulation contrast.

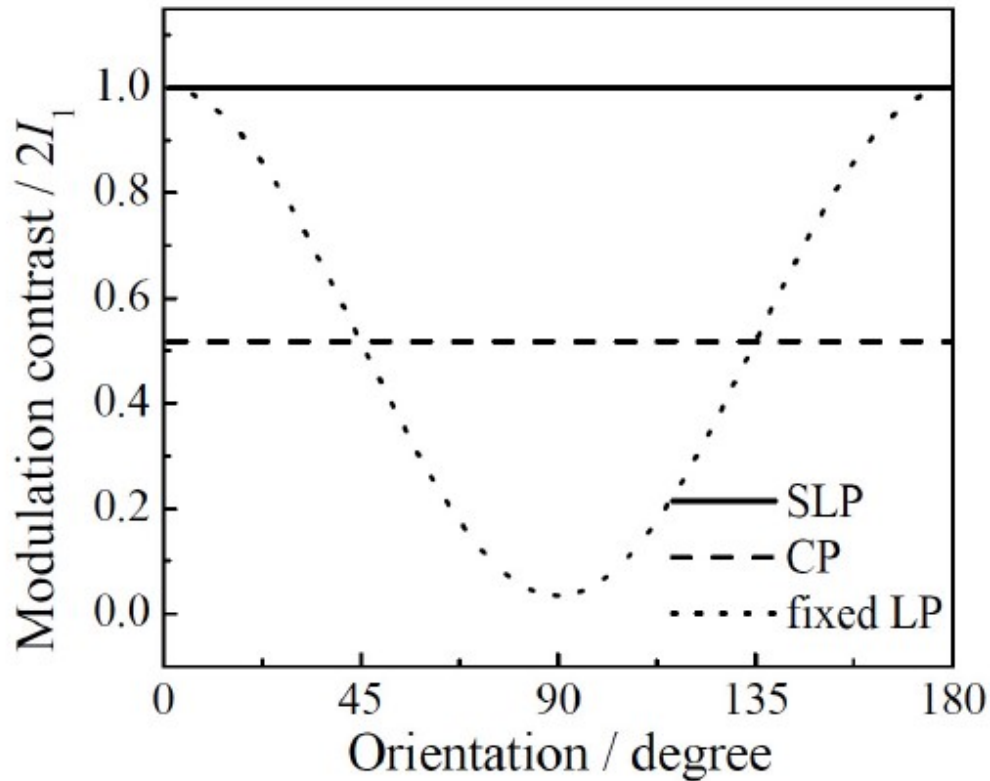


Figure 3-11: The relation between the orientation of linearly polarized light and the modulation contrast. The modulation contrast of three cases are compared here: SLP where the ideal linear polarization is maintained, the case of circular polarization on the sample plane and a fixed orientation linear polarization. As the pattern orientation is changed, the fixed linear polarization decreases in modulation depth, dependent on alignment with the orientation of the pattern.

Source: Huang et al. [17]

To maximize modulation contrast, polarization control is applied in the illumination path of the optical setup to align the linear polarization with the direction of the sinusoidal pattern.

3-5-1 Aligning the polarization

We use a Meadowlark liquid crystal variable retarder (LCVR) to change the polarization to align with the diffraction direction. To rotate the polarization 90 degrees, Meadowlark advises to use the LCVR in combination with a quarter wave plate. To do so, the fast axis of the LCVR should be under an 45° angle to the incoming polarization. Next, the slow axis of the quarter wave plate should be aligned with the orientation of the original polarization state. By using a retardance of a half wavelength, we can rotate the polarization state with 90° .

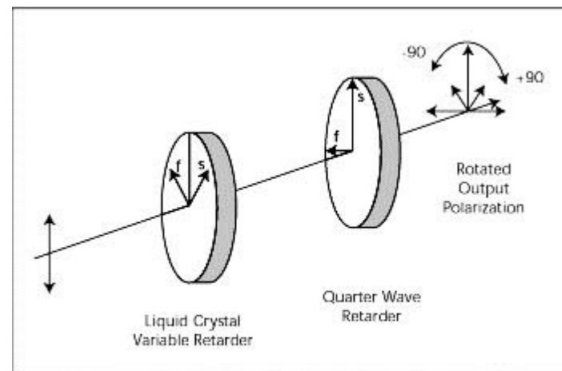


Figure 3-12: Schematic overview of the integration of the LCVR. The fast angle of the LCVR is placed under an angle of 45° to the incoming polarization state. The slow axis of the QWP is aligned to the incoming polarization direction. Using the LCVR controller, the angle of the exiting polarization state is rotated.

Source: Meadowlark Optics polarization solutions

As the LCVR gives a minimum retardance of 30nm , we need to change the retardance between half wavelength and full wavelength, rather than zero and half wavelength retardance. This will give the same desired outcome, as a full wave retardance does not result in a change of polarization.

3-6 Timing of the imaging experiment

To execute an experiment with a sequence of phase-shifted illumination patterns, we need to address the timing schedule. The design of the optical setup enables for 9 phase shifts per orthogonal direction. To create non-equidistant phase shifts, we do not use all these projections, but only one third, as we show in chapter five. These three phase steps in the two directions of illumination need to be executed within the "ON"-time during which a fluorescent molecule emits light. Currently, the camera limits the frame rate of the entire experiment to 440fps. This means that 6 frames will take a minimum of 13ms if we use the maximum frame rate.

Chapter 4

Experimental methods

In order to evaluate the resolution improvement, we create a benchmark for SMLM by building a TIRF microscope setup with uniform illumination. In addition, we compare the TIRF microscope performance with a similar TIRF setup to get an idea of the performance of our setup quality. We also use this TIRF microscope to image the fluorescent samples for on-time analysis. Next, we describe the process of calibration of the excitation focus of the SIM beams. Finally, we describe the on-time measurements for fluorophores.

4-1 Benchmarking SMLM

4-1-1 Comparison of TIRF setups

We built a custom PALM-TIRF setup similar to the work of Kwakwa et al. in [1] and compared it to the SIMFLUX setup in standard SMLM experiments. We show this custom PALM-TIRF setup in figure 4-1.

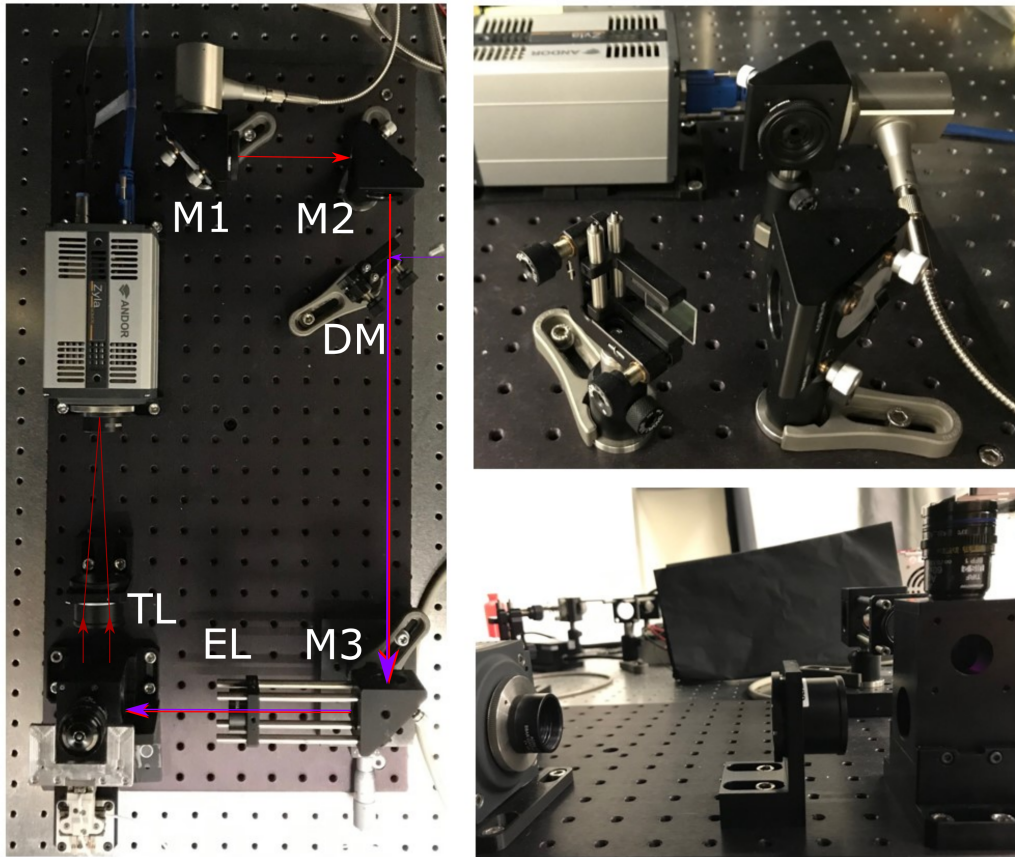


Figure 4-1: Figure of the custom PALM-TIRF setup that we built. Left: a beam collimator points the light into M1 and M2 (top). The dichroic mirror transmits the red light and accepts the UV path in a reflective way. M3 mounted on a linear stage directs the light in the microscope tower. By moving the stage the illumination can be changed from epifluorescence to TIRF microscopy. From the sample plane, the emission light is magnified by the objective and focused by the tube lens into the camera. Top right: close-up of the dichroic mirror to add the UV-laser into the microscope light path. Bottom right: close-up of the Olympus tube lens, used to focus the emission light from the objective into the camera.

We use Alexa-647 dye to compare the localization precision of this setup with the SIMFLUX setup (in homogeneous illumination mode) and create a benchmark for SMLM. The process of sample preparation is described in section four. We set the illumination power to 8mW on the sample plane to match the configuration to the imaging settings of the dataset we received from the SIMFLUX setup, in order to create an honest comparison between the two setups. This results in a set of emission spots with similar photon counts. For the SIMFLUX setup, $\langle N \rangle = 421, 4$, $\langle bg \rangle = 2, 85$. For the custom PALM-TIRF setup, $\langle N \rangle = 504, 5$, $\langle bg \rangle = 8, 22$.

Comparison of two microscope towers Additionally, we measure the effect of internal reflections in the objective tower by comparing two microscope towers: the one in figure 4-1 is black by an anodizing layer and has an exit hole behind the mirror for transmitted light. The first version of the microscope design is a standard aluminium part with no hole for stray light

that was transmitted through the mirror. We show the differences between the two towers in figure 4-2:

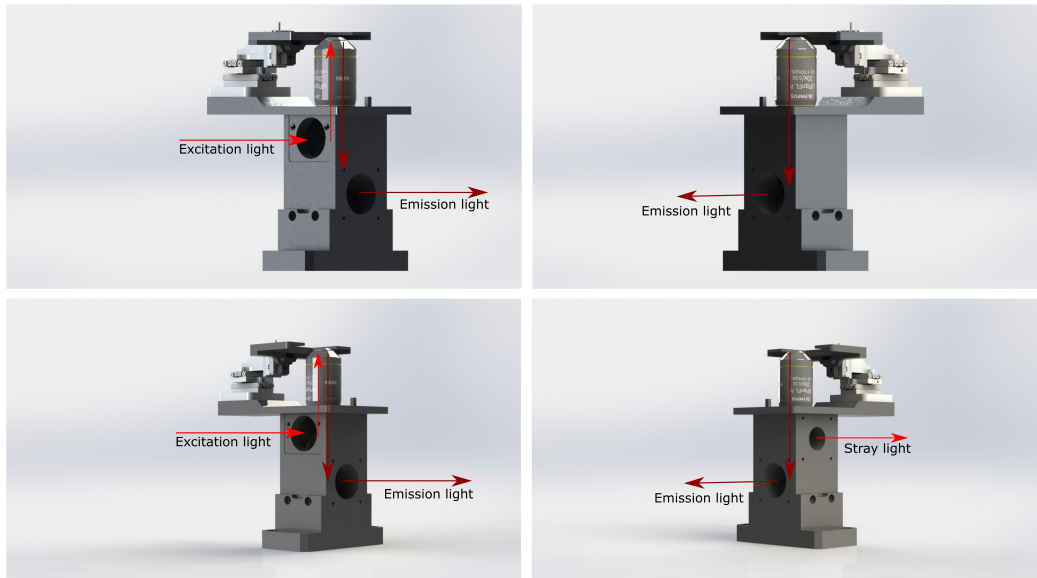


Figure 4-2: Renders of two versions of the microscope tower. Top: the first prototype of the microscope tower with no exit hole for laser light that was transmitted through the mirror. As the tower is milled from aluminium and this version has no coating, the surfaces are highly reflective. Bottom: in the updated model, an exit hole for stray light is milled. Furthermore, the surface areas have a black anodizing layer.

Rejection of laser speckle We also compared two different approaches to reject the influence of laser speckle in the multi-mode laser. In the first approach, we use a rotating glass diffuser to reject speckle from the laser. In the second approach, we reduce the beam size to reject the influence of speckle during experiments. This is a separate experiment with an illumination power that deviates from the previous comparison.

Comparison of two laser sources Finally, we compare the effect of interchanging the laser sources. We use the Toptica single-mode laser source with a design wavelength of 640nm and a maximum power of 200mW. The second laser source is a multi-mode laser source from Changchun New Industries (CNI) with a design wavelength of 640nm and a maximum power of 2000mW.

4-1-2 Analysis of precision

Camera calibration

The camera we use is an Andor Zyla scientific complementary metal oxide semiconductor (sCMOS) with a pixel size of $6.5\mu\text{m}$. The camera can be calibrated using the fact that the relation between the photon count and the variance of the read-out noise is linear. For this

calibration, we use the work of Van Vliet et al. in [18]. Using measurements of the covered-up sensor, we can establish the offset. Using measurement data with a wide variety of intensities, we can assess the relation between photon count and read-out noise. Given these values, we calibrate the offset and gain of the camera. In this routine, we limit the maximum intensity being used in the fit to 3000, as slight non-linearities are introduced beyond this intensity. Figure 4-4 shows the outcome of the camera calibration.

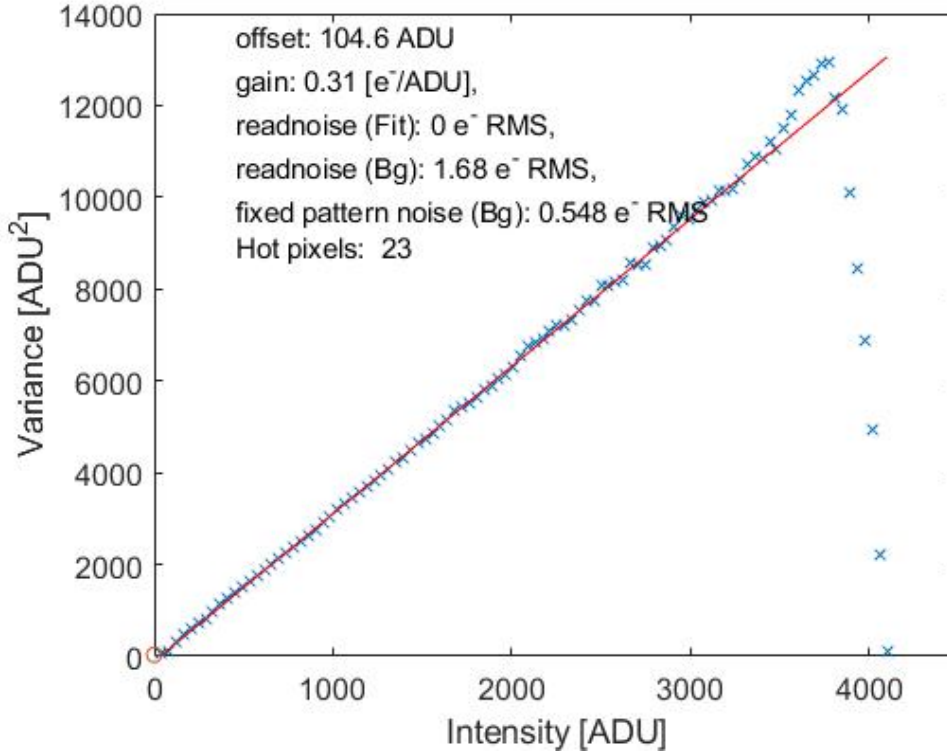


Figure 4-3: Camera calibration of the DMD setup

Theoretical precision of measurements

After compensating for the gain and offset of the camera, we start the localization of emission spots using the maximum likelihood estimation routine, like we described in section two. The output parameters of the fitting process are spatial positions, intensity and background level and finally the width of the Gaussian PSF σ_g . Rieger et al. present the following analytical description of the localization precision, based on the CRLB of the estimation in their work [6]:

$$\Delta x_{loc}^2 = \frac{\sigma_e^2}{N} \left(1 + 4\tau + \sqrt{\frac{2\tau}{1 + 4\tau}} \right), \quad (4-1)$$

where $\sigma_e^2 = \sigma_g^2 + a^2/12$, $\tau = 2\pi\sigma_g^2 b/Na^2$, a is the sample plane pixel area and b is the number of background photons per pixel.

4-2 Calibration of the DMD-SIM setup

4-2-1 Aligning the excitation focus

The alignment of the excitation focus is done according to the work of Young et al. [19]. In this work, they show how the focal plane is found where the interference of the two beams is in focus. Although they use a spatial light modulator to create the required diffraction patterns, the process is very similar. Subsequently, they ensure the focus of the excitation path has the same optical depth as the focus of the emission path. Figure 4-4 shows the process of finding the excitation focus and potential alignment errors.

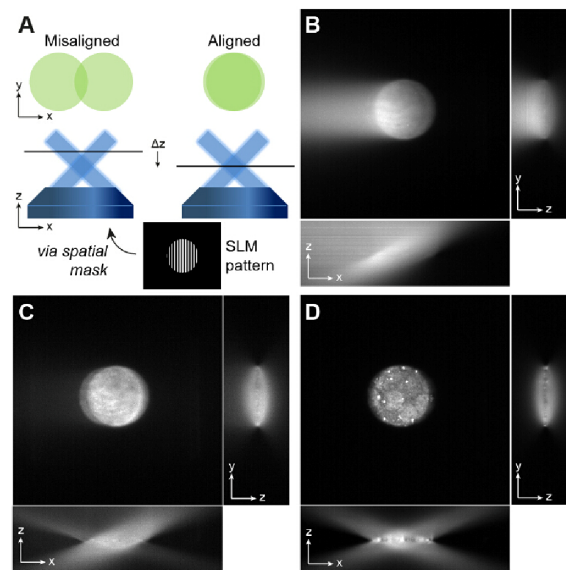


Figure 4-4: A) The alignment of the excitation plane with the emission plane is done by finding the location where the two beams completely overlap. B) When a bright streak like this is visible, the critical angle for TIRF is not achieved. C) Both beams have the required angle for TIRF, but the beams don't overlap entirely. Only in the overlapping section will be the required interference for patterned illumination. D) When the beams are completely aligned, the camera will be repositioned in order to focus the emission path on this plane.

We show the process of finding the overlapping of these two beams in our setup in figure 4-5:

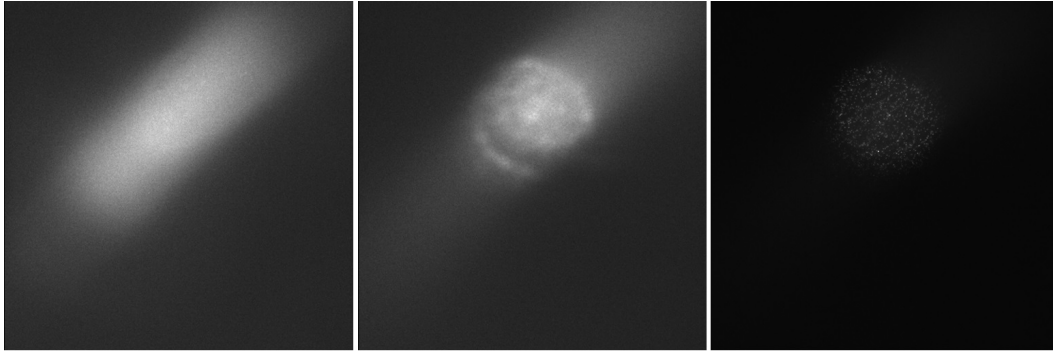


Figure 4-5: Finding the right axial position of the SIM pattern. A high density fluorescent bead sample is used to image the excitation pattern of the SIM setup. Left: the two beams are not overlapping at all and both form a streak of light. Middle: part of the beam is overlapping, creating a region with an elevated intensity level. On both sides, streaks of light are still visible. Right: the two beams overlap almost entirely, with only a small streak of light on the right side of the illumination spot.

4-2-2 Distribution of illumination energy in back focal plane

When the incident angle of the DMD is not correct, the envelope of the DMD diffraction does not align with the diffraction of the pattern [10]. This results in an uneven energy distribution among the two diffraction peaks. If this is the case, the modulation depth of the illumination pattern will deteriorate. In figure 4-6 we compare the distribution of laser power as a way to assess the incident angle of the DMD. We do this by reading out a camera that images the back focal plane of the objective, like we show in figure 4-6:

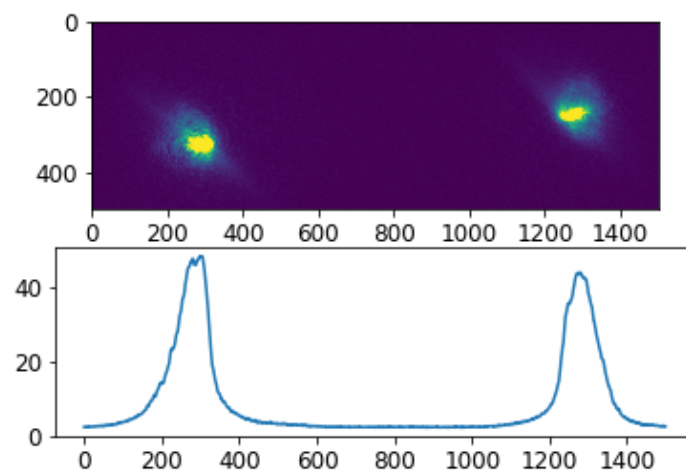


Figure 4-6: The blaze angle can be found by comparing the intensities of the diffraction peaks in the back focal plane of the objective. Top: cropped camera image from the back focal plane camera. Bottom: mean intensity over column of pixels.

The distance between these spots should measure $2 \cdot 4.17 = 8.34\text{mm}$. With the pixel size

of $3.45\mu\text{m}$, the expected distance is $\frac{2 \cdot 4.17}{3.45 \cdot 10^{-3}} = 2417$ pixels apart. However, to measure both diffraction spots within the detector range of the back focal plane camera, the distance between the peaks was modified. We show that the peaks are in the designed location through the spatial filter. We designed the spatial filter based on the simulations and we can conclude that the two diffraction peaks are transmitted, whereas the center peak is entirely blocked out.

4-2-3 Calibration of the pitch and phase of the illumination pattern

Estimation of the illumination pattern

We estimate the pattern pitch by projecting the different patterns on a high density fluorescent sample. The localizations of all fluorescent spots result in position-dependent intensities. We derive the pattern pitch by applying the Fourier transform to all these spots, resulting in two peaks for each direction in the Fourier domain. This is shown in figure 4-7.

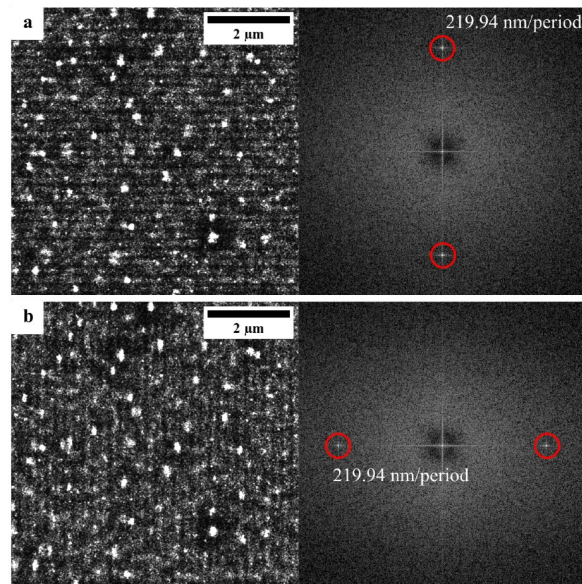


Figure 4-7: Pattern estimation by applying the Fourier transform to the localization data of a high density fluorophore sample. a) Left: initial localization of spots with structured illumination in y -direction. Right: The Fourier transform of the localizations of these spots, resulting in two sharp peaks indicating the pattern pitch in y -direction. b) Left: initial localization of spots with structured illumination in x -direction. Right: like in a), the Fourier transform of the localizations of the data from results in two sharp peaks indicating the pattern pitch in x -direction.

Source: Localization microscopy at doubled precision with patterned illumination [9].

Defining the phase and modulation depth of the illumination pattern

After we define the spatial frequency of the periodic pattern, we can use the initial localizations to derive the phase and modulation depth. We do this by applying a least square fit to the sample plane intensity distribution, using the localization coordinates and intensities as

sampling points for the function. For this estimation, we use equation 2-11 and 2-14 for two directions:

$$\min_{\psi_x, m} \|Y_x - (1 + m \cos 2\pi q_x \cdot x - \psi_x)\|_2^2, \quad (4-2)$$

$$\min_{\psi_y, m} \|Y_y - (1 + m \cos 2\pi q_y \cdot y - \psi_y)\|_2^2. \quad (4-3)$$

Here, Y_x, Y_y are the localized coordinates with the corresponding intensities as sampling points for the sinusoidal patterns that are fitted. One thing to take into account is that this could potentially create problems for PA-SIMFLUX, as we expect that mainly low intensity spots are fitted. Therefore part of the sinusoidal function would not be sampled. We need to assess if this is really a problem after completion of building the setup.

4-2-4 Calibration of the activation pattern

When the DMD is used for mapping an image from the DMD plane to the sample plane, the calibration we perform for the illumination path is not appropriate. In order to assess the quality of the mapping, we use a checkerboard pattern. By using a high density sample we can show the mapping of the DMD pattern to the sample plane.

4-3 On-time analysis of fluorophores

To define the time window in which all the phase steps of the illumination pattern need to be completed, we need to know the on-time of a fluorophore. In STORM and PALM, a fluorescent molecule blinks between an "ON" state and a temporary "OFF" state, before switching to a permanent dark state. The "ON"-time is defined to be the time that a blinking fluorophore emits light before turning to the dark state and can be found by analyzing the blinking data of fluorescent molecules. In the setup, we compare the on-time of the commonly used STORM dye Alexa-647 with the photoactivatable dye Janelia Fluor646 (PA-JF646), as these are directly available for use. Figure 4-8 shows the excitation and emission spectra of the two fluorescent dyes, as well as the reflectivity of the dichroic mirror towards the camera.

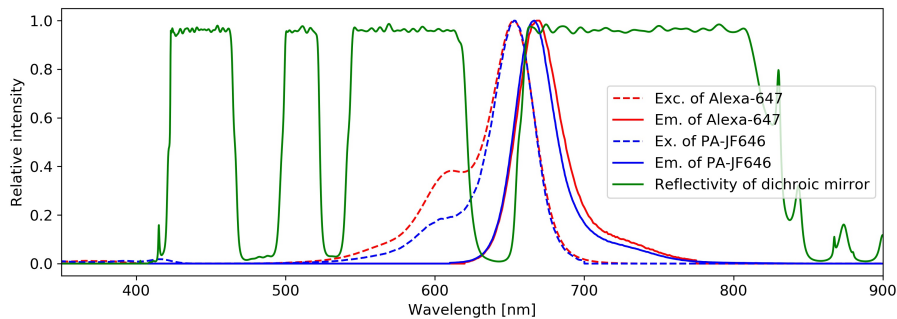


Figure 4-8: Spectra of fluorescent dyes and dichroic mirror. The excitation- and emission spectra of Alexa-647 and PA-JF646 highly overlap. Both peaks of the emission spectra are reflected by the dichroic mirror to be reflected through the tube lens into the camera.

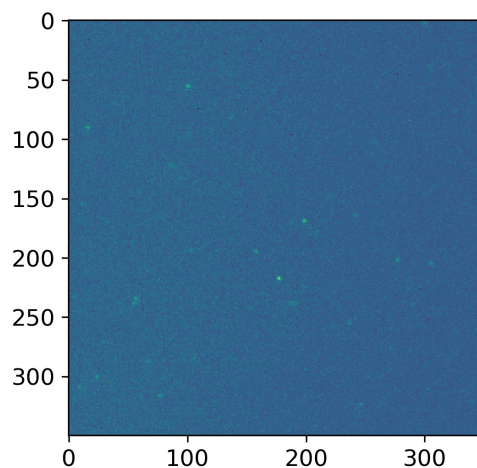


Figure 4-9: Single frame of the blinking data from a 350x350 pixel field of view. This image capture was taken from the STORM data.

In figure 4-9 we show an example of the captured data. By localizing each individual spot and counting the consecutive frames in which the same coordinates are found, localizations can be combined. This is done manually for a selection of spots, as well as by using the localization analysis for the entire data set. In the latter, we combine spots that have a separation of less than 0.5 pixels (about two times the CRLB for Gaussian localization) and skip a maximum of 1 frame. We compare experiments with different illumination power.

4-3-1 Sample preparation

In dSTORM, activation of fluorescent dyes happens spontaneously in a stochastic manner. To maintain a long fluorescent lifetime, the sample buffer needs to be optimized. Fluorescent dye transfers to a dark state due to the presence of oxygen in a solution. Therefore, in an efficient STORM buffer an oxygen scavenger is needed. Furthermore, the acidity of the solution needs to remain stable and have a pH value of around 8,4. The most commonly used STORM buffer is Glucose Oxidase (GLOXY)[20]. Glucose oxidase removes the oxygen from the solution. However, as byproduct of this process hydrogen peroxide is produced, which affects the performance of the fluorophores. Therefore, Catalase is added to remove the hydrogen peroxide. The buffer is separated into four subsolutions, as the ultimate buffer solution remains stable for a limited time [20]. We describe the process of creating the buffer solution in way to store it for a long time in appendix A. In appendix B we cover the preparation for STORM and PALM samples.

Chapter 5

Results

In this chapter we discuss the results from the experiment that we did. We begin with the comparison of the TIRF setups, where the different configurations of the custom PALM-TIRF setups are covered as well. Next, we discuss the analysis of the on-time of both fluorescent dyes and the feasibility to use them in modulation enhanced localization microscopy. Finally, we present the expected improvement in localization precision through simulation of the CRLB.

5-1 Comparison of TIRF setups

We show the results of the comparison in localization precision in table 5-1:

Table 5-1: Comparison of localization precision

Configuration	Localization precision (nm)
SIMFLUX setup	$6,61 \pm 0,82$
PALM-TIRF, reflective tower	$12,89 \pm 0,89$
PALM-TIRF, anodized tower	$10,11 \pm 0,93$

We notice a significant difference in localization precision between the custom built PALM-TIRF setup and the SIMFLUX setup. As reason for this, we notice the significant difference in background photons and the change in pixel size: although the SIMFLUX setup worked with the same camera setup, the magnification of the system was 100x instead of 60x for the PALM-TIRF setup. This results in a camera plane pixel size of 65nm and 108nm respectively. This difference is squared in the pixel area, which deteriorates the localization precision as the sampling of the PSF model is less detailed.

Furthermore, we notice an improvement of localization precision by using the black anodized microscope objective tower. This can be explained by the fact that not all laser light is being reflected into the objective. What is transmitted through the laser, can cause internal reflection, ultimately increasing the background level of the measurements.

Table 5-2 shows the results of the comparison between the two laser sources:

Table 5-2: Comparison of performance between two laser sources

Configuration	Localization precision (nm)
Toptica single-mode	14.51 ± 1.0
CNI multi-mode	14.74 ± 0.31

We do not conclude a significant difference in localization precision between the multi-mode laser from CNI or the single-mode laser from Toptica, indicating that both laser sources can be interchanged in the PALM-TIRF setup without consequence.

Next, we present the results of the comparison between the two different approaches to reject laser speckle in table 5-3.

Table 5-3: Comparison of approaches to reject laser speckle

Configuration	Localization precision (nm)
Rotating glass diffuser	$12,98 \pm 0,83$
Beam size reduction	$19,10 \pm 0,92$

We compare two approaches to reject the laser speckle that bled through the spectral filters onto the camera. First, we executed an imaging experiment using a rotating glass diffuser. This rejects interference of modes that cause local bleed-through. A second approach to reject this problem is by reducing the beam size. The processed data clearly shows a significant improvement when using the rotational beam diffuser.

5-2 On-time analysis

5-2-1 On-time of Alexa-647

We measure the on-time of Alexa-647 at different power levels. Figure 5-1 shows the on-time, counted by hand and figure 5-2 shows the results from the localization software.

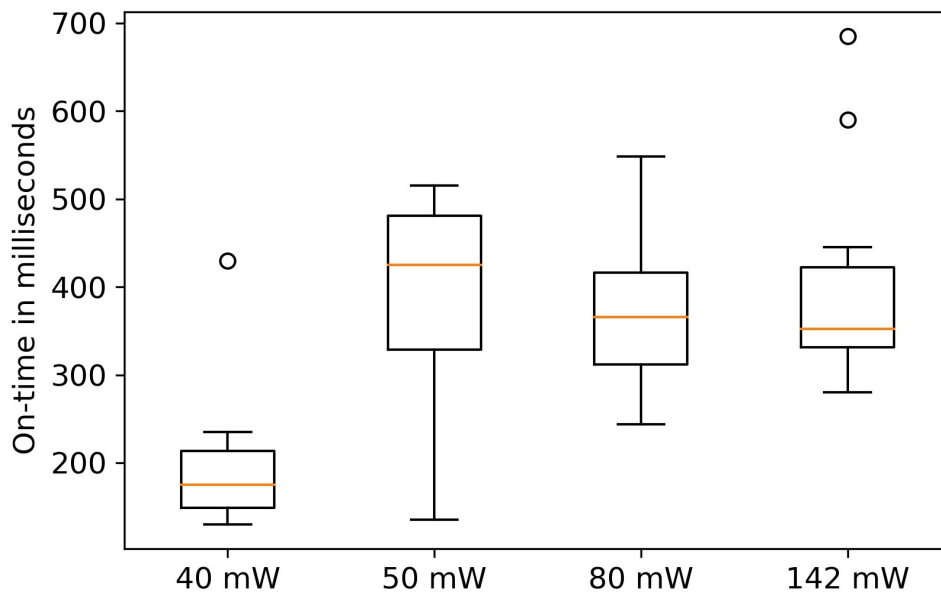


Figure 5-1: On-times of STORM dye Alexa-647 with Glucose Oxidase buffer, measured by manually counting a selection of emission spots.

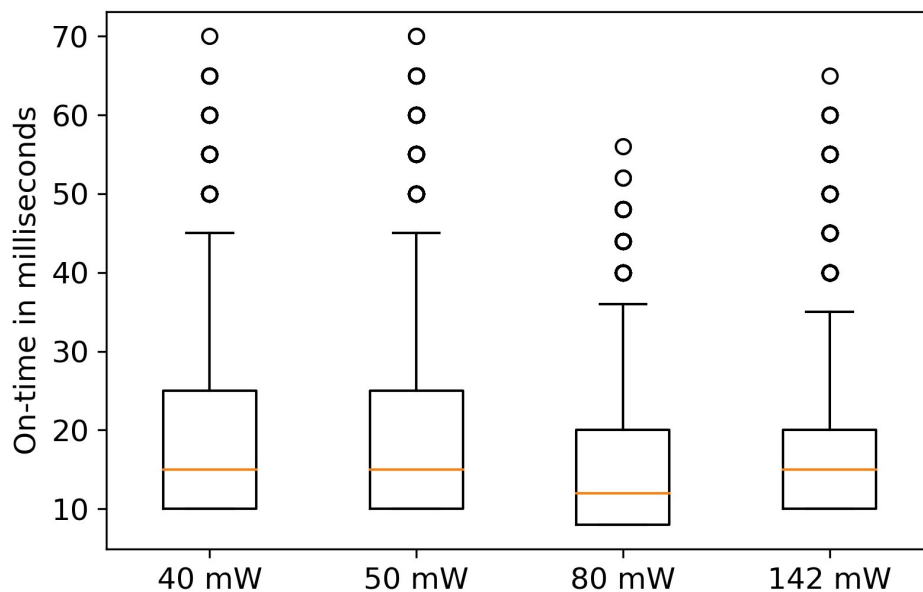


Figure 5-2: On-times of STORM dye Alexa-647 with Glucose Oxidase buffer, processed using localization software.

We notice a very large difference between the manually determined on-time and the outcome when we use the localization software. This is due to the high amount of events where an emission spot is illuminated for only two or three frames. This will drive down the mean on-time significantly. When counting by hand, these events are easily missed when playing

the data file as a movie. This explains the higher outcome of on-time analysis if we measure by hand. The Wilcoxon rank-sum test confirms that the manually selected spots and the processed spots do not have the same underlying distribution. We show the p-value of the hypothesis that the distributions of the compared data sets are equal in table 5-4:

Table 5-4: Wilcoxon rank-sum test on STORM data. The low p-values indicate that the distributions of the manually selected spots and the localized data are not equal.

Measurement	p-value
40mW	$4.62e^{-8}$
50mW	$4.58e^{-8}$
80mW	$4.65e^{-8}$
142mW	$4.37e^{-8}$

When we look into previous work for reference, we find that Zhao et al. present a mean on-time of 100ms for Alexa-647 in [21]. The measurements in this work are done with a different buffer solution, which could explain the difference.

5-2-2 On-time of PhotoActivatable JF-646

The on-time of the manually counted selection of Janelia dye PA-JF646 is shown in figure 5-3 and in figure 5-4 we show the results from the localization data:

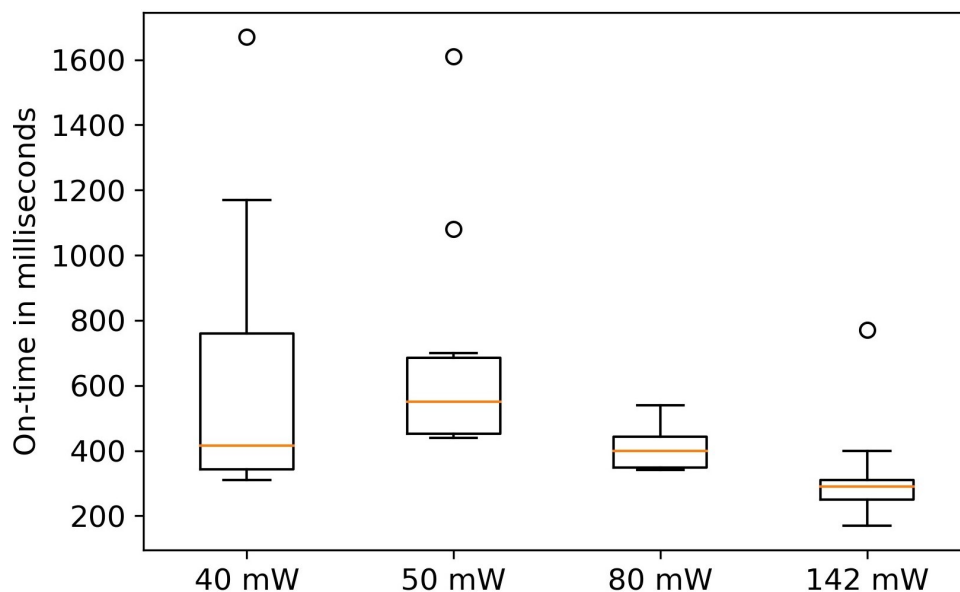


Figure 5-3: On-times of PALM dye PA-JF646 with PBS, measured by manually counting a selection of emission spots.

Again, we notice a large difference between the manually selected spots and the total amount of processed spots with the localization software. The Wilcoxon rank-sum test in table 5-5 confirms that the distributions are not equal.

Table 5-5: Wilcoxon rank-sum test on PALM data. The low p-values indicate that the distributions of the manually selected spots and the localized data are not equal.

Measurement	p-value
40mW	$7.94e^{-8}$
50mW	$4.42e^{-8}$
80mW	$4.79e^{-8}$
142mW	$5.63e^{-8}$

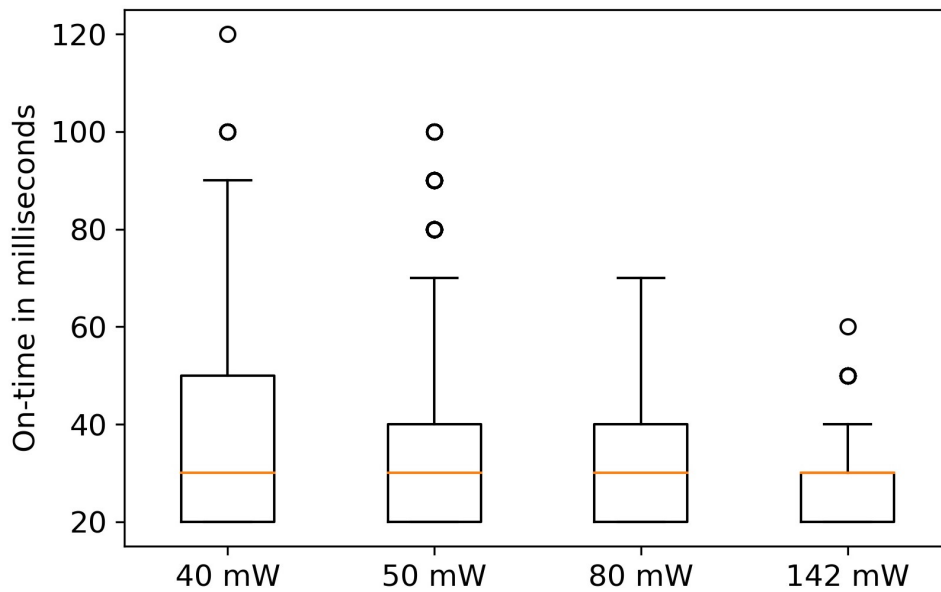


Figure 5-4: On-times of PALM dye PA-JF646 with PBS, processed using localization software.

5-2-3 Feasibility for use in modulation enhanced localization microscopy

When we compare the on-times of Alexa-647 and PA-JF646, we notice a slight increase in on-time. This makes the photo-activation dye more appropriate for imaging experiments like these, even when no patterned photo-activation is desired. When we want to use a fluorescent dye for an imaging experiment, we want the on-time sufficiently long to project the complete set of patterns, but not much longer. If the on-time of a fluorescent dye is too long, this will result in a large portion of overlapping emission spots [22]. Since the fluorescent on-time varies per molecule, we can experience two scenarios. When the on-time of a molecule is too short to project all the illumination patterns, we need to discard these measurements for the processing of modulation enhanced improvement. When the on-time of a molecule is longer than the time needed for this experiment, the emission spot of that molecule could be overlapping with a new blinking event and would also need to be discarded. Figure 5-2 shows the distributions of on-time for the STORM dye Alexa-647. For the maximum amount of phase steps in this setup, we need to project 18 patterns during the on-time of the fluorophore, requiring 41ms. Since the on-time is a constraint here, one idea to overcome this is by using a smaller amount of illumination patterns, resulting in a shorter required time window to

complete an imaging experiment. This, as we showed previously will decrease the resolution improvement.

For the PA-SIMFLUX experiment, a total of six exposure events of the DMD are simulated to project the phase steps of the pattern, three in each direction. With the camera frame rate limited to 440fps, this results in a full cycle of projections in 13ms. Figure 5-4 shows the distributions of the entire data sets for the photo-activatable dye. We can conclude that a majority of the blinking spots has an on-time above 13ms and will therefore be suitable for the experiment.

5-3 Simulations of precision improvement with DMD setup

Since we have not been able to execute imaging experiments with the designed TIRF-SIM setup yet, here we present the expected improvement using the currently designed pattern pitch. The pattern is created with a DMD pitch of 9 pixels. Thus, a shift of one pixel corresponds with a phase step of one ninth of the full pitch, i.e. 40 degrees. We create a high resolution region of one third of the pitch, i.e. 120 degrees. Therefore, we use three patterns with a relative phase shift of 40 degrees. We show the designed improvement with perfect modulation contrast in figure 5-5:

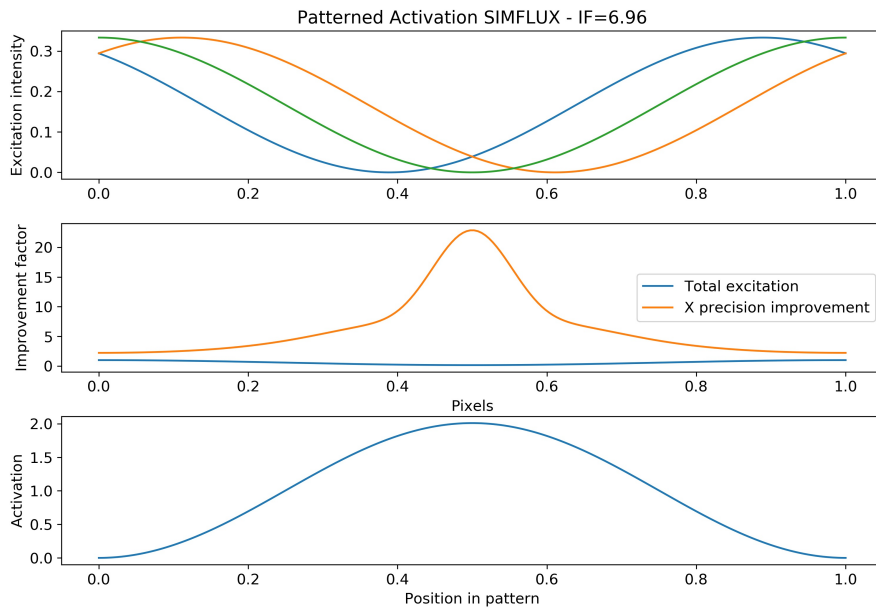


Figure 5-5: Simulated improvement with perfect modulation contrast. Top: the different illumination patterns with phase steps that are not distributed equally over the full period of the pattern. Middle: the blue line shows the sum of these excitation patterns, the orange line shows the position-dependent precision improvement. Bottom: the patterned photoactivation is aligned with the region of maximum precision improvement.

For this simulation, we use an intensity of 1000 photons in combination with 10 background

photons. This results in a CRLB for uniform illumination of 9.40nm . With perfect modulation, the mean improvement factor is 6.96 , corresponding with a CRLB of 1.35nm . With a non-ideal modulation contrast, this of course will be lower. If the modulation contrast decreases, the improvement factor will be lower. We show the cases for a modulation contrast of 0.95 in figure B-2 and a modulation contrast of 0.90 in figure 5-7. Here, the mean improvement factors are 5.64 and 4.78 , corresponding with a mean CRLB of 1.67nm and 1.97nm .

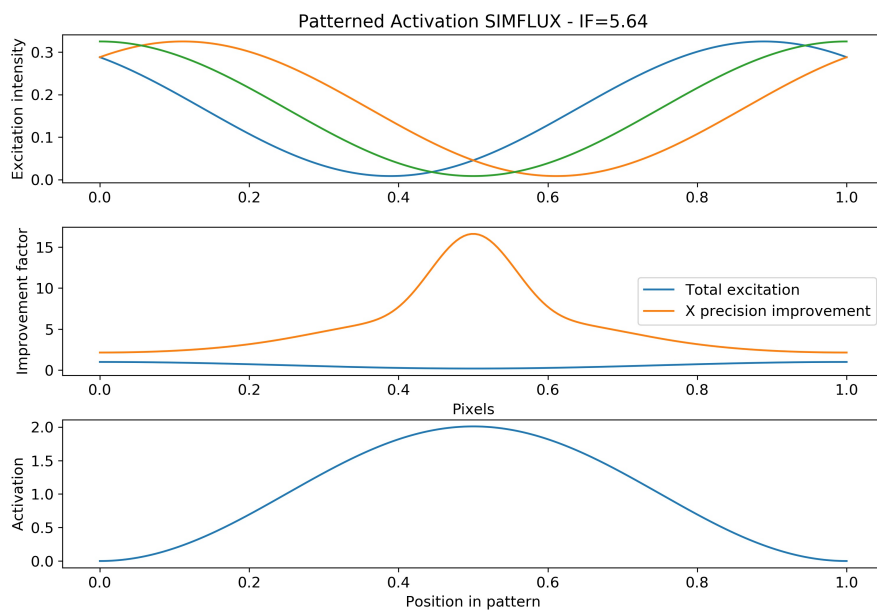


Figure 5-6: Simulated improvement with a modulation contrast of 0.95 . Top: the three excitation patterns are always non-zero due to non-ideal modulation contrast. Middle: this results in total excitation intensity that is not constant over the field of view. Bottom: Again, we activate the region with a local peak in precision improvement using an activation pattern that has an identical pitch to the excitation pattern.

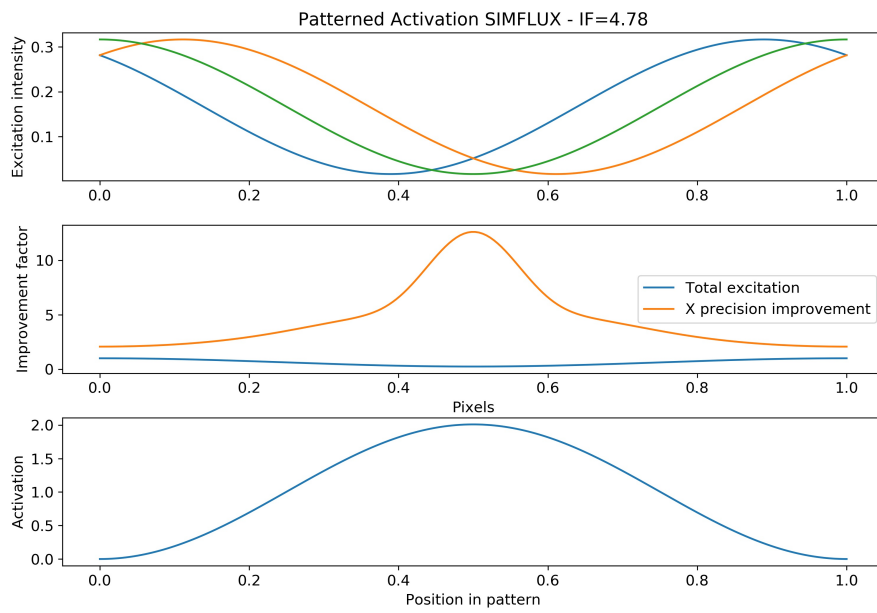


Figure 5-7: Simulated improvement with a modulation contrast of 0,90. Middle: the effect of non-ideal becomes more apparent in the plotted total excitation power.

Chapter 6

Roadmap to alignment

In this chapter we present a plan to cope with alignment problems that up to now we have not been able to solve.

6-1 Laser coupling alignment

A stable light spectrum is achieved by a constant illumination power. If it is necessary to dim the power, this should be done by rotating a half wave plate (HWP) in combination with a polarizer. We collimate the light by placing a collimation lens exactly one focal distance away from the fiber coupling. For this, we use an achromatic doublet with a focal length of 75mm. This results in a beam diameter of $2 \cdot 75 \cdot NA_{fiber} = 150 \cdot 0.08 = 12mm$. A pinhole is placed behind this collimator lens to adjust the beam size. We measure the collimation by using the shear-plate interferometer. A z-axis translation mount (SM1Z) is used to ensure collimation of the beam. The fiber coupling is placed with an XY-movement mount on the cage system. We can use this to align the center of the Gaussian shaped beam with the center of the pinhole. Figure 6-1 shows the setup for the fiber coupling and collimation of the light beam.



Figure 6-1: Fiber coupling of the illumination laser. From left to right, we see the single-mode fiber coupled into the fiber coupling on an XY-mount at the start. Next, the post to elevate the fiber coupler to the optical path height. Furthermore, we use a lens mount with precise linear motion in the axial position to place a collimation lens ($f = 75\text{mm}$). After the lens, we placed an adjustable iris to adjust the beam size. Far right, we see a half-wave plate to control the laser illumination power.

6-2 Ensure linear polarization and controlling the polarization state

The laser has a linearity with an extinction ratio greater than 100:1. We can clean this polarization state by implementing a Glan-Laser polarizer (Thorlabs, GL10-A), which has an extinction ratio of 100,000:1. A Glan-Laser polarizer discards all but one polarization direction, resulting in highly polarized light. This Glan-Laser polarizer should be placed on a rotation mount, in order to enable control of the exiting polarization state. By using a calibrated iris to ensure the height of the incoming and exiting light (polarized and non-polarized), we can ensure the orientation of the polarization state of the exiting beam. Since the laser is linearly polarized to begin with, we can use a HWP before the Glan-Laser polarizer to rotate the incoming polarization state and, using this method, control the laser power. Since mirrors introduce a phase lag [23], it is advised to minimize the amount of mirrors used in the system, while maintaining the ability to align the optical path. The broadband dielectric mirrors that are often used, are more sensitive to polarization-dependent phase lag and thus polarization change. Therefore, we advise to use silver or aluminium mirrors for ideal performance.

To investigate the polarization change caused by birefringence of the DMD and its protection glass cover, we can use the method we discussed in section three to assess the polarization state of the incoming beam and the reflected beam of the DMD. One of the problems we encountered previously was that a change in polarization also affected alignment. A potential cause for this is that the angle of incidence (AOI) of one of the polarization optics is not zero. It is best to ensure 0-degree AOI by steering back-reflection into the beam, ideally over a long distance. It is also advised to place polarization optics in collimated beam paths to avoid AOI deviations.

6-3 Aligning the optical path

After ensuring that any change in polarization does not affect the alignment of the beam, the optical path can be established. To do this, all the pixels of the DMD must be activated to create one spot. By using a pair of irises that have been calibrated for the optical path height, we can ensure the optical path between the DMD and the dichroic mirror is horizontal. This is important to prevent angle of incidence dependent aberrations when the lenses are placed. When we decrease the size of the laser beam using an adjustable iris, an Airy pattern is formed. This is maintained by the DMD, resulting in a beam shape that has clear distinguishable rings of zero intensity, like we showed previously in figure 1-3. We use these rings to align the center of the beam with the two pinholes.

The final part of the optical path alignment is done with the dichroic mirrors and the mirror underneath the objective. This is possible because the required corrections will be very small. By placing a temporary cage system on top of the objective mount, irises can be placed on different heights to ensure the optical path is ultimately vertical. Since the objective is fixated in its mount, the optical path should not only be vertical, but also perfectly in the center of the objective mount.

6-4 Positioning the lenses

When the optical path is correctly aligned, we place the lenses in the system. To do this, we work from the objective to the DMD. First the objective is placed in its mount. Secondly, the excitation lens is placed. We use linear translation mounts for the lenses in order to correct for minor deviations from the optical path. The lens mount is placed on a linear stage to reach the correct axial alignment of the lens. This is assessed by looking at the exit beam of the objective. This should be again centered in the cage system and collimated. Since the exit beam of the objective is too small to use the shear-plate interferometer, we use optical path length to assess whether the beam is diverging or collimated. Because the focal length of the objective is so small, this is a realistic way to assess the axial position of the excitation lens. To prevent lens-induced aberrations, we place a piece of paper with a small hole right after one of the previously mentioned pinholes. Using this method, we can observe the back reflection of the lens and correct for angle of incidence errors. After placing the excitation lens, we remove the objective and place the second lens with a focal length of 50 mm. Using the shearplate-interferometer and the previously mentioned methods, we can assess the position of this two lens system. Before placing the last lens, the objective is placed back in its position. By doing so, we create a four lens system, resulting again in a collimated exit beam pointing into the column.

6-5 Ensuring equal intensity distribution

By optimizing the DMD incidence angle, as discussed in Chapter two, we can distribute the laser power evenly over the diffraction peaks. In practice, it is a good idea to ensure equal intensities by dimming the higher intensity beam with a neutral density filter or LP filter [24].

6-6 Assessment of polarization at sample plane

To measure the polarization state of the exiting beam, we can place a LP above the objective and establish linear polarization. This can be done with the zero order of the diffraction pattern, which should be centered through the objective. Using the QWP after the DMD, we can correct for linearity of the polarization. Using the HWP after the DMD, we can correct for the orientation of the linear polarization state. Ultimately, the modulation depth of the illumination pattern should be optimized. As discussed in chapter 4, this should be done using experiments with a high density fluorescent sample.

Conclusions and outlook

7-1 Conclusions and outlook

7-1-1 Conclusion

Single molecule localization microscopy is a powerful tool for researchers to image live cells with super-resolution. Recently, the introduction of structured illumination patterns enabled image reconstruction with a single nanometer localization precision range.

With the use of structured illumination, the localization precision varies over the field of view. During this project, we showed the potential resolution improvement of single molecule localization microscopy with a mean improvement factor of 4.78 compared to the case of uniform illumination with a realistic modulation depth. This can be achieved by using non-equidistant phase steps in structured illumination, exploiting the local peak in precision improvement by patterned activation of this region.

We designed a PALM setup using two digital micromirror devices to create TIRF-SIM capabilities with an excitation pitch of 231nm and an activation pitch of 233nm and started the build of this setup. To finish this setup, we wrote an alignment plan to cope with potential problems. To create a benchmark, we built a custom TIRF-PALM setup and executed experiments with an expected localization precision of 10.11nm with an intensity of 500 photons. This custom TIRF-PALM setup was also used to do on-time measurements of the fluorescent dyes that we have available. For the sample preparation, we created a buffer solution for STORM dyes using Glucose Oxidase. We analyzed the on-time of Alexa-647 and PA-JF646, to conclude on feasibility. The photo-activation dye can be used, but in DMD-SIMFLUX for STORM dyes, we need to adjust the amount of phase steps. An alternative would be to select a different dye for future experiments.

7-1-2 Outlook

Apart from finishing the build of this setup and proving the precision improvement on real data, this project leads to several possibilities. As we have shown in figure 3-5, the emission

path of the microscope is very basic and all the additional information comes from the illumination path of the microscope. This gives rise to the opportunity to optimize the shape of the PSF towards three-dimensional imaging [25] or multiple-emitter fitting [26]. Another potential line of research would be the inclusion of the SwissSPAD. Currently, the system speed is limited by the camera frame rate. SwissSPAD is a new single photon avalanche diode (SPAD) array with an extremely high frame rate of 6.1kfps. This enables high frame rate imaging with changing illumination patterns, supported by the 22 kHz frame rate of the Vialux V-7000 DMD for 1-bit images.

Appendix A

Protocol for Glucose Oxidase buffer

We separate the catalase solution, the glucose oxidase solution, a buffer base solution and ultimately the working buffer solution.

Glucose oxidase solution freezer stocks: This solution can be stored at -20°C .

- $50\mu\text{L}$ of 1M NaCl
- $20\mu\text{L}$ of 1M Tris at 7.4 pH
- $0.7\mu\text{L}$ of -ME stock
- $429.3\mu\text{L}$ of Nanopure water
- $500\mu\text{L}$ of 100% glycerol anhydrous
- 135mg glucose oxidase from *Aspergillus Niger* Type VII, lyophilized powder, ($\geq 100,000$ units/g) solid

Catalase solution freezer stocks: This solution can be stored at -20°C .

- $50\mu\text{L}$ of 1M NaCl
- $20\mu\text{L}$ of 1M Tris at 7.4 pH
- $0.7\mu\text{L}$ of β -ME stock
- $429.3\mu\text{L}$ of Nanopure water
- $500\mu\text{L}$ of 100% glycerol anhydrous
- 50mg Catalase from bovine liver ($\geq 10,000$ units/mg)

Buffer base solution: This solution can be stored at 4°C.

- 2.5mL 1M Tris at 8.0 pH
- 2.5mL 1M NaCl
- 25mL of 20% Glucose (autoclaved)
- 19.5mL of Nanopure water

Working buffer solution: This solution should be used instantly.

- 958μL of the base buffer
- 10μL of Glucose oxidase stock
- 2μL of Catalase stock
- 30μL of β-ME stock

Appendix B

Sample preparation

B-1 Aliquotting dry photo-activatable fluorophores

The photoactivatable Janelia FLuor 646 (PA-JF₆₄₆) was delivered as dry substance. In order to use it, it needs to be dissolved to create a high concentration stock solution. To plan for long-term storage, the high concentration stock dissolution is done in dimethyl sulfoxide (DMSO), so that it can be stored at -20°C without damage to the fluorescent dye. Each package contains 100nM particles. Dissolving in 100 μ L DMSO gives 1,00mM of dyes. We dilute 1 μ L of this solution 100 times by adding 99 μ L DMSO, resulting in a stock solution of 10 μ M.

B-2 Sample preparation

For the sample preparation, procedures for STORM and PALM dyes are similar. The buffer solution that is used for the STORM dye Alexa-647 is the previously described Glucose Oxidase (GLOXY), whereas we use phosphate buffered saline (PBS) with a pH of 8.4 for the PALM dye PA-JF646.

1. Dilute the dye with ethanol to a concentration of $10^{-11}M$
2. Distribute 10 μ L of poly-L-lysine over the cover slip and let sit for a minute. Remove the residu using pipet
3. Distribute 15 μ L solution of fluorescent dye solution on cover slip
4. Let dry while protecting it from light by covering with e.g. aluminium foil
5. Tape the cover slip to a sample slide
6. Fill cavity between cover slip and sample slide using 35 μ L of buffer solution

7. Seal the edges of the cover slip using Picodent Twinsil®

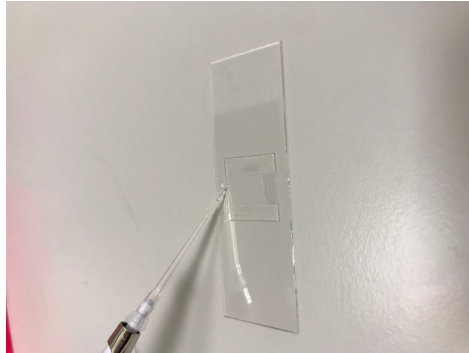


Figure B-1: Filling the volume between the cover slip and the sample glass with buffer solution.

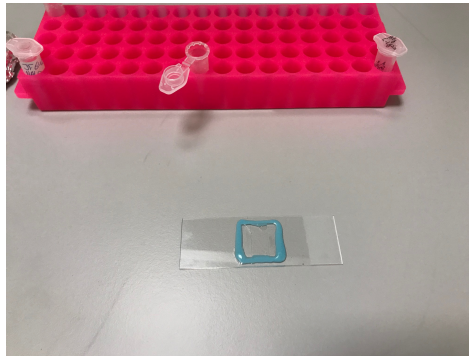


Figure B-2: Sealing off the sample with Picodent to prevent oxygen from entering the solution.

Bibliography

- [1] K. Kwakwa, A. Savell, T. Davies, I. Munro, S. Parrinello, M. A. Purbhoo, C. Dunsby, M. A. Neil, and P. M. French, “easySTORM: a robust, lower-cost approach to localisation and TIRF microscopy,” *Journal of Biophotonics*, vol. 9, pp. 948–957, Sept. 2016.
- [2] S. Shashkova and M. Leake, “Single-molecule fluorescence microscopy review: shedding new light on old problems,” *Bioscience Reports*, vol. 37, p. BSR20170031, Aug. 2017.
- [3] M. J. Rust, M. Bates, and X. Zhuang, “Sub-diffraction-limit imaging by stochastic optical reconstruction microscopy (STORM),” *Nature Methods*, vol. 3, pp. 793–796, Oct. 2006.
- [4] S. T. Hess, T. P. Girirajan, and M. D. Mason, “Ultra-High Resolution Imaging by Fluorescence Photoactivation Localization Microscopy,” *Biophysical Journal*, vol. 91, pp. 4258–4272, Dec. 2006.
- [5] C. S. Smith, S. Stallinga, K. A. Lidke, B. Rieger, and D. Grunwald, “Probability-based particle detection that enables threshold-free and robust in vivo single-molecule tracking,” *Molecular Biology of the Cell*, vol. 26, pp. 4057–4062, Nov. 2015.
- [6] B. Rieger, R. Nieuwenhuizen, and S. Stallinga, “Image Processing and Analysis for Single-Molecule Localization Microscopy: Computation for nanoscale imaging,” *IEEE Signal Processing Magazine*, vol. 32, pp. 49–57, Jan. 2015.
- [7] K. N. Fish, “Total Internal Reflection Fluorescence (TIRF) Microscopy,” *Current Protocols in Cytometry*, vol. 50, Oct. 2009.
- [8] K. Kwakwa, A. Savell, T. Davies, I. Munro, S. Parrinello, M. A. Purbhoo, C. Dunsby, M. A. Neil, and P. M. French, “easySTORM: a robust, lower-cost approach to localisation and TIRF microscopy,” *Journal of Biophotonics*, vol. 9, pp. 948–957, Sept. 2016.
- [9] J. Cnossen, T. Hinsdale, R. Thorsen, M. Siemons, F. Schueder, R. Jungmann, C. S. Smith, B. Rieger, and S. Stallinga, “Localization microscopy at doubled precision with patterned illumination,” *Nature Methods*, vol. 17, pp. 59–63, Jan. 2020.

- [10] A. Sandmeyer, M. Lachetta, H. Sandmeyer, W. Hübner, T. Huser, and M. Müller, “DMD-based super-resolution structured illumination microscopy visualizes live cell dynamics at high speed and low cost,” preprint, Biophysics, Oct. 2019.
- [11] C. S. Smith, N. Joseph, B. Rieger, and K. A. Lidke, “Fast, single-molecule localization that achieves theoretically minimum uncertainty,” *Nature Methods*, vol. 7, pp. 373–375, May 2010.
- [12] S. Stallinga and B. Rieger, “Accuracy of the Gaussian Point Spread Function model in 2D localization microscopy,” *Optics Express*, vol. 18, p. 24461, Nov. 2010.
- [13] C. S. Smith, N. Joseph, B. Rieger, and K. A. Lidke, “Fast, single-molecule localization that achieves theoretically minimum uncertainty,” *Nature Methods*, vol. 7, pp. 373–375, May 2010.
- [14] M. Bierbaum, B. D. Leahy, A. A. Alemi, I. Cohen, and J. P. Sethna, “Light Microscopy at Maximal Precision,” *Physical Review X*, vol. 7, p. 041007, Oct. 2017.
- [15] J. W. Goodman, *Introduction to Fourier Optics*. Roberts & Company Publishers, 3rd edition ed., 2005.
- [16] K. O’Holleran and M. Shaw, “Polarization effects on contrast in structured illumination microscopy,” *Optics Letters*, vol. 37, p. 4603, Nov. 2012.
- [17] H.-C. Huang, B.-J. Chang, L.-J. Chou, and S.-Y. Chiang, “Three-beam interference with circular polarization for structured illumination microscopy,” *Optics Express*, vol. 21, p. 23963, Oct. 2013.
- [18] L. J. van Vliet, D. Sudar, and I. T. Young, “Digital Fluorescence Imaging Using Cooled CCD Array Cameras invisible,” p. 14, 1998.
- [19] L. J. Young, F. Ströhl, and C. F. Kaminski, “A Guide to Structured Illumination TIRF Microscopy at High Speed with Multiple Colors,” *Journal of Visualized Experiments*, p. 53988, May 2016.
- [20] L. Nahidiazar, A. V. Agronskaia, J. Broertjes, B. van den Broek, and K. Jalink, “Optimizing Imaging Conditions for Demanding Multi-Color Super Resolution Localization Microscopy,” *PLOS ONE*, vol. 11, p. e0158884, July 2016.
- [21] T. Zhao, Y. Wang, Y. Zhai, X. Qu, A. Cheng, S. Du, and M. M. T. Loy, “A user-friendly two-color super-resolution localization microscope,” *Optics Express*, vol. 23, p. 1879, Jan. 2015.
- [22] J. Xu, H. Ma, and Y. Liu, “Stochastic Optical Reconstruction Microscopy (STORM),” *Current Protocols in Cytometry*, vol. 81, July 2017.
- [23] M. Delay, “Practical Aspects of Mirror Usage in Optical Systems for Biology.”
- [24] L. Reymond, J. Ziegler, C. Knapp, F.-C. Wang, T. Huser, V. Ruprecht, and S. Wieser, “SIMPLE: Structured illumination based point localization estimator with enhanced precision,” *Optics Express*, vol. 27, p. 24578, Aug. 2019.

- [25] C. Smith, M. Huisman, M. Siemons, D. Grünwald, and S. Stallinga, “Simultaneous measurement of emission color and 3D position of single molecules,” *Optics Express*, vol. 24, p. 4996, Mar. 2016.
- [26] E. Nehme, D. Freedman, R. Gordon, B. Ferdman, L. E. Weiss, O. Alalouf, T. Naor, R. Orange, T. Michaeli, and Y. Shechtman, “DeepSTORM3D: dense 3D localization microscopy and PSF design by deep learning,” *Nature Methods*, vol. 17, pp. 734–740, July 2020.

